Boundary-Layer Meteorology (2023) 187:229–265
https://doi.org/10.1007/s10546-023-00797-y

RESEARCH ARTICLE

# Subgrid Variability of Atmospheric Surface-Layer Parameters in Complex Terrain

**Sebastian F. Otarola Bustos[1] · Harindra J. S. Fernando[1] · James M. Wilczak[2] · Andrey A. Grachev[3] · Christopher Hocut[3] · Robert Dumais[4]**

Received: 18 February 2022 / Accepted: 13 February 2023 / Published online: 28 March 2023


**Abstract**
This paper reports analysis of eddy-covariance data collected during the WFIP2 field campaign in the complex-terrain of the US Pacific Northwest. A 31-day period representative of the region's dry season was used to address the following questions: (1) To what extent does the Constant-Flux Layer (CFL) assumption hold? (2) What is the spatial variability of turbulent and momentum fluxes over km scales? and (3) How skilful are the surface-layer parameterizations of mesoscale models? These questions are directly relevant to subgrid parameterization studies of mesoscale models. Results show that the efficacy of the CFL concept and the spatial variability of turbulent and momentum fluxes are dependent on: (i) the turbulent parameter being analysed, (ii) the measurement's location, (iii) the atmospheric stability regime (determined by the flow and vertical stratification), and (iv) the magnitude of the flux. Finally, the skill of the physics formulation of an often-used surface-layer parameterization scheme available in the Weather Research and Forecasting (WRF) model was also evaluated. Meteorological conditions associated with the highest and the lowest errors were identified. A metric to quantify (time-dependent) flow heterogeneity is proposed, which appears to be a good candidate to predict the skill of idealized surface-layer parameterization schemes in complex terrain.

**Keywords** Constant-flux layer · Complex terrain · Parameterizations · Subgrid variability · Surface-layer

✉ Sebastian F. Otarola Bustos
sotarola@nd.edu

1 Department of Civil and Environmental Engineering and Earth Sciences, University of Notre Dame, Notre Dame, IN, USA

2 Physical Sciences Laboratory, NOAA, Boulder, CO, USA

3 Boundary Layer Research Team/Atmospheric Dynamics & Analytics Branch, DEVCOM Army Research Laboratory, White Sands, NM, USA

4 Data Assimilation and Nowcasting Team, Army Research Laboratory, Adelphi Las Cruces,, NM, USA

## 1 Introduction

Complex-terrain flows cover multiple space–time scales and are associated with steep gradients of meteorological variables that depend on the complexity of the terrain and background forcing (Fernando 2010). Complex terrain weather has many societal applications, such as, prediction of air quality (Giovannini et al. 2020), aviation hazards (Gultepe et al. 2019), wildfire control (Carvalho et al. 2020), agricultural damage from frost due to cold pooling (Chung et al. 2006), wind energy (Haupt et al. 2019), and anomalous rainfall and flooding (Luchetti et al. 2020). These applications rely on mesoscale Numerical Weather Prediction (NWP) models that use 1–30 km horizontal grid sizes, where atmospheric motions such as fronts, tropical storms, land/sea breeze, mountain/valley circulation, and thunderstorms can be captured (Sati and Mohan 2021). Yet, microscale (1–100 m) turbulent eddies within the Atmospheric Boundary Layer (ABL) that are key to the exchange of momentum, heat, and mass in the atmosphere are not properly represented in NWP models (Maronga et al. 2020). In particular, terrain heterogeneities (complex terrain) pose challenges for accurately calculating turbulent fluxes of momentum, heat, and moisture in the Atmospheric Surface Layer (SL) (Martins et al. 2009; Liang et al. 2020), wherein important interactions between the surface and air aloft takes place (Wouters et al. 2012). Terrain heterogeneities can modify surface drag, turbulent mixing, and heat transfer, and they can interact with the background flow at multiple space–time scales, generating a wide range of meteorological phenomena including but not limited to internal boundary layers, thermal winds, critical layers, lee waves, and rotors (Garrat 1994; Fernando et al. 2010; Kadivar et al 2021).

In NWP models, turbulent fluxes as well as winds, temperature, and moisture at the lowest computational level are represented using physics-based expressions known as Surface Layer parameterization schemes (hereafter SL schemes) (Stull 1988; Nakanishi and Niino 2009; Jiménez et al.2012). These SL schemes rely on the assumed presence of a Constant-Flux Layer (CFL) where turbulent fluxes of momentum, heat, and moisture are approximately constant, and the existence of a CFL is the basis of the Monin–Obukhov Similarity Theory (MOST) developed for Flat and Homogeneous Terrain (FHT) (Obukhov 1946; Monin and Obukhov 1954). The terms Surface Layer (SL) and CFL are used in the literature interchangeably. Even for nearly idealized FHT in nature, turbulent fluxes change with height, and their vertical gradients often peak near the ground where turbulent fluxes tend to be the highest. As pointed out by Wyngaard (2011), nonetheless, when non-dimensionalized by SL scales, these gradients become negligible, and hence the name CFL.

In practice, over FHT, where the applicability of MOST has been well established (Panofsky and Dutton 1984; Wyngaard 2011), a CFL is said to exist over the height where turbulent fluxes vary less than 10% (Kaimal and Businger 1970). Nonetheless, SL schemes are employed for all types of terrain, including complex terrain, for which only a few authors have explored the validity of the CFL approximation. For instance, Nadeau et al. (2013) studied the vertical variability of turbulent heat and momentum fluxes over a steep alpine slope (25°–40°) near La Fouly, Switzerland, and Sfyri et al. (2018) did the same (with the addition of water vapor fluxes) for the Inn Valley, Austria. They both reported variations in turbulent fluxes that exceed by an order of magnitude validity thresholds commonly used for MOST. Nadeau et al. (2013) used a 10% threshold for the first 6 m above the ground, and Sfyri et al. (2018) used a 20% threshold for the first 20 m above the ground (which was used in this study). Dan Li et al. (2018) found that when a CFL is assumed in the Atmospheric Surface Layer, several constraints are imposed on high-order fluxes and their gradients, thus

understanding when the CFL breaks down in complex terrain is of great importance, not only for its obvious impact on the skill of SL schemes.

This article uses eddy-covariance data obtained in an area of complex terrain of horizontal dimensions comparable to a single grid cell of a mesoscale model (∼1 to 3 km) during the Second Wind Forecast Improvement Project (WFIP2) field campaign (Wilczak et al. 2019) to address three research questions: (1) To what extent does the CFL approximation hold in complex terrain? (2) What is the horizontal spatial variability of turbulent heat and momentum fluxes in the area studied, which is within subgrid scales of mesoscale models, and (3) Is the Monin–Obukhov (MO) theory developed for FHT and used by SL schemes in NWP models capable of representing the friction velocity for the entire instrumented site, and under what conditions it tends to fail?

## 2 Methods

### 2.1 Dataset

The data analyzed and discussed herein were obtained during the WFIP2 experiment that took place in the Columbia River gorge and basin region of the US Pacific Northwest (OR and WA) between 2015 December and 2017 January. Specifically, the three components of wind velocity and sonic temperature were obtained with an array of meteorological towers equipped with multiple levels of sonic anemometers (at 20 Hz). The vertical profiles of wind speed and direction up to 200 m above ground level (agl) were measured with a SODAR (hereafter, for brevity, agl will not be used when describing the heights).

The instruments covered a region of complex terrain comparable to the horizontal dimensions of a single grid cell of a high-resolution Numerical Weather Prediction (NWP) model ($\Delta X$, $\Delta Y$ $\sim$ 1 to 5 km). This region was located ~ 8 km southwest from Rufus (OR) and 5 km North from Wasco (OR). The layout of the towers and the terrain elevation are given in Fig. 1a. The elevation profile of the tower transect for T1, T2, T6, and T11 (indicated by the red line in Fig. 1a) is shown in Fig. 1b. The 10-m tower and the SODAR at site T1 are shown in Fig. 2a, and the 21-m tower at site T6 is shown in Fig. 2b. This transect had an approximately East–West (EW) direction, and it spanned a distance ~ 2.6 km, characterized by an average slope of 5% and an elevation difference of 40 m. Figure 1a and b were generated using terrain data with 1/3 arc seconds (~ 10 m) horizontal resolution downloaded from the National Elevation Dataset (NED) at https://nationalmap.gov. The exact coordinates, terrain elevation, type of instrumentation, and measurement heights are listed in Table 1 for all sites. Additional details regarding the T1 observation site (Physics Site PS01), the instrumentation, and the data can be found in Grachev et al. (2020, 2022).

### 2.2 Data Quality Control

As listed in Table 1, the operation of towers in Fig. 1 was done by multiple research organizations. To minimize uncertainties associated with different tower operators, the raw data for all towers were processed using the same quality control procedures developed for the University of Notre Dame (UND) towers. This included sequentially: (i) visual inspection of data, (ii) removal of outliers, defined as points with differences higher than four standard deviations from the median, and (iii) tilt correction using the planar-fit method that aligns the sonic anemometer coordinate system into a mean streamline coordinate system to reduce

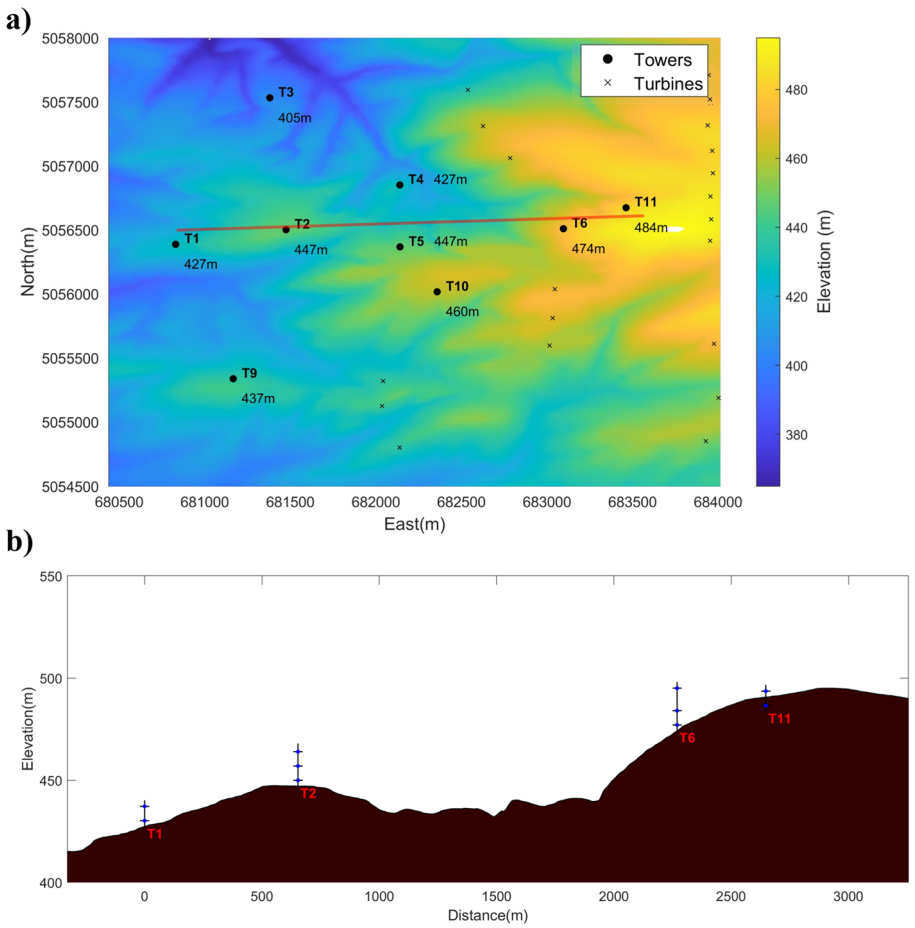


**Fig. 1** **a** Colormap of Elevation for the instrumented region. Towers and wind turbines are indicated by the circle and cross symbols, respectively, and the local terrain elevation is indicated for all tower sites. **b** Elevation profile for East–West transect of UND towers (red line in Fig. 1a)

crosswind errors when calculating fluxes (Wilczak et al. 2001). In addition, to minimize wake effects from the towers and wind turbines located in the eastern part of the domain (Fig. 1a), only data associated with wind direction in the sector 240°–290° was used in the statistical analysis of Sects. 3.2 and 3.3.

### 2.3 Micrometeorological Conditions During Study Period

For this study, a 31-day period between 27 August to 26 September, 2016 was selected in view of (i) the availability of a complete dataset from the towers and SODAR, (ii) presence of dry soil conditions for ABL turbulence studies, and (iii) ideal meteorological conditions for the study of CFL validity and the evaluation of SL schemes, which were identified with selected values of wind speed, wind direction ($\theta$), and Obukhov length $L$, with the latter

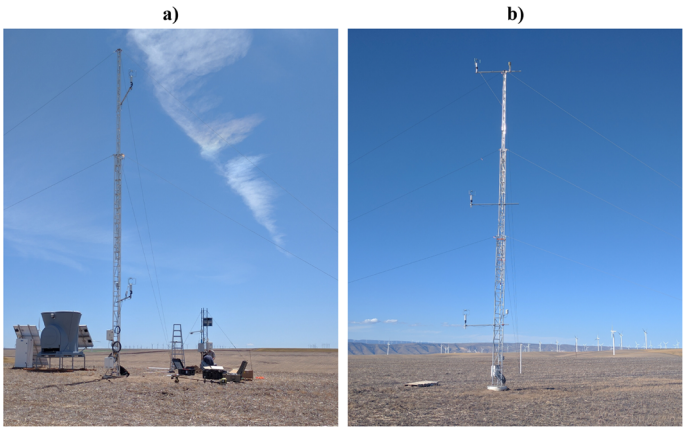


**Fig. 2** **a** ND tower T1 with two levels of sonic anemometers and co-located instrumentation of collaborators (SODAR and solar/soil measurements). **b** ND tower T6 with three levels of sonic anemometers

**Table 1** Tower's location, height, and elevation in meters above sea level (masl)

| Tower | LAT | LON | Elevation (masl) | Sonic levels (m) | Model | Deployed by |
|---|---|---|---|---|---|---|
| T1 | 45.637 | − 120.679 | 428 | 3, 10 | Young RM 8100 | University of Notre Dame (UND) |
| T2 | 45.638 | − 120.672 | 445 | 3, 10, 17 | | |
| T6 | 45.6378 | − 120.651 | 475 | 3, 10, 21 | | |
| T11 | 45.6394 | − 120.646 | 484 | 3, 10 | | |
| T3 | 45.648 | − 120.673 | 405 | 10 | Metek USA-1 | Argonne National Laboratory (ANL) |
| T9 | 45.628 | − 120.676 | 439 | 10 | | |
| T4 | 45.641 | − 120.663 | 426 | 10 | Gill R3-50 | Pacific Northwest National Laboratory (PNNL) |
| T5 | 45.6369 | − 120.663 | 449 | 10 | | |
| T10 | 45.6337 | − 120.661 | 458 | 10 | | |

defined according to Eq. 1:

$$L = -\frac{u_*^3}{\kappa g \alpha Q_T}, \tag{1}$$

$$u_* = \left(\overline{u'w'}^2 + \overline{v'w'}^2\right)^{\frac{1}{4}}, \tag{2}$$

$$Q_T = \overline{w'T_s'}, \tag{3}$$

$$\alpha \cong \overline{T_s}^{-1}, \tag{4}$$

where $u_*$ is the friction velocity (defined in Eq. 2), $Q_T$ is the turbulent temperature flux (defined in Eq. 3), $\alpha$ is the thermal expansion coefficient (defined in Eq. 4), $\kappa$ is the von Kármán constant, and $g$ is the gravitational acceleration.

The terms $\overline{u'w'}$ and $\overline{v'w'}$ in Eq. 2 correspond to the longitudinal and lateral momentum fluxes, respectively. The overbar operator indicates the covariance of high-frequency quantities ($u\prime w\prime$, $v\prime w\prime$, and $w\prime T_s\prime$) over a 15-min interval, with ($u'$, $v'$, $w'$) and ($T_s'$) velocity and temperature fluctuations measured with sonic anemometers, respectively.

In Fig. 3a–c, the black dots correspond to 15-min averaged wind speed, wind direction (theta) calculated from the averaged wind components, and Obukhov length at z = 10 m and spatially averaged across all 9 towers, $\langle V \rangle$, $\langle \theta \rangle$, and $\langle L \rangle$, respectively. The spatial variability of the measurements ($\langle \cdot \rangle \pm \sigma_x$) is indicated by the light-blue shaded region.

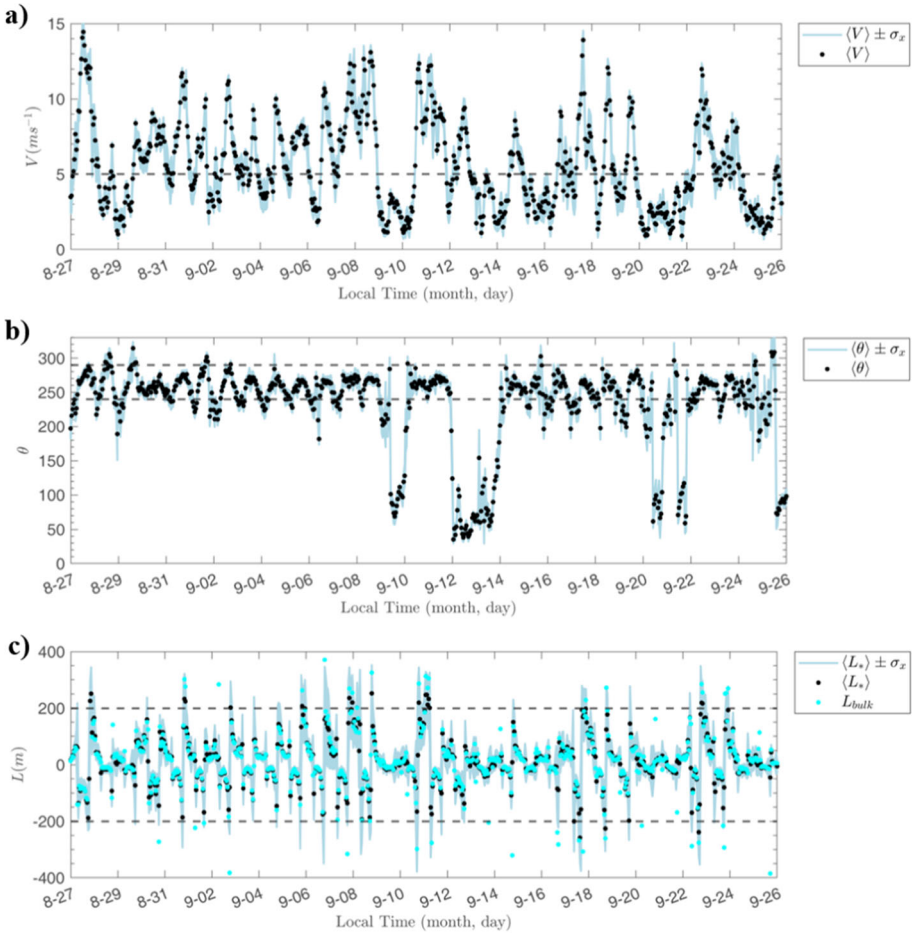


**Fig. 3** Time series of **a** wind speed, **b** wind direction, and **c** Obukhov length. The angular brackets ⟨.⟩ indicate the variables ($V$, $\theta$, or $L$) were averaged in space across all 9 towers (black dots in **a**–**c**).The light-blue shaded area corresponds to the spatial standard deviation of measurements across all 9 towers ($\sigma_x$). The cyan dots in **c** correspond to a *'bulk'* Obukhov length $L_{bulk}$. The data was smoothed with a 1-h averaging window for convenience of visualization

**Table 2** Stability classification based on Obukhov length scale ($L$) threshold and stability parameter at z = 10 m

| Class of flow | Obukhov length ($\boldsymbol{L}^*$) | Stability parameter ($\boldsymbol{\xi} = \boldsymbol{z}\boldsymbol{L}^{-1}$) |
|---|---|---|
| Unstable (U), | When $-200 \leq L < 0$ | $\xi \leq -0.05$ |
| Stable (S) | When $0 < L \leq 200$ | $\xi \geq 0.05$ |
| Neutral (N) | When $\|L\| > 200$ | $-0.05 < \xi < 0.05$ |

The ideal meteorological conditions selected from the 31-day period used in this study included (i) identifiable quiescent and transitional winds separated by a windspeed threshold of 5 m $s^{-1}$ (dashed line in Fig. 3a), (ii) frequent westerly winds in attendance and defined by wind directions in the sector 240°–290° (indicated by the two dashed lines in Fig. 3b), and (iii) three distinct stability regimes based on the Obukhov length at z = 10 m and consistent with previous studies (Moraes et al. 2005; Tampieri et al. 2009; Munoz-Esparza et al. 2012; Sfyri et al. 2018; Bodini et al. 2019), as indicated in Table 2.

In Table 2, $L$ is the Obukhov length in meters (Eq. 1), and threshold values $L = \pm 200$ m are indicated by the two dashed lines in Fig. 3c.

To illustrate the spatial variability of the Obukhov length within spatial scales comparable to the finest grid-cells of mesoscale models, a bulk Obukhov length ($L_{bulk}$) was calculated according to Eq. 5, which is analogous to Eq. 1, but with spatially averaged values of $u_*$, $Q_T$ and $\alpha$ across all towers, as indicated by the angular brackets:

$$L_{\text{bulk}} = -\frac{\langle u^* \rangle^3}{\kappa g \langle \alpha \rangle \langle Q_T \rangle}, \tag{5}$$

where $\langle u^* \rangle$ is the observed friction velocity spatially averaged across all 9 towers and calculated according to Eq. 6 as:

$$\langle u^* \rangle = \frac{1}{N} \sum_{i=1}^{N} u^*(x_i, t). \tag{6}$$

And $u^*(x_i, t)$ is the friction velocity at z = 10 m measured at site $x_i$ (with $i = 1, 2, \ldots, N$), with $N = 9$ the number of towers. Similarly, $\langle \alpha \rangle$ and $\langle Q_T \rangle$ are the spatially averaged thermal expansion coefficient and temperature flux across all 9 towers. Given the similarity of $\langle u^* \rangle$ to the definition of $L_{bulk}$, $\langle u^* \rangle$ can be thought of as a 'bulk' friction velocity.

The values of $L_{bulk}$ (cyan dots in Fig. 3c) are in general agreement with the spatially averaged values of $L$ (black dots in Fig. 3c); however, note that during periods of high variability between the towers (high $\sigma_x$), differences between $L$ and $L_{bulk}$ can be important. The reasons of these differences are beyond the scope of this article and call for more detailed studies in complex terrain at small horizontal scales (1–3 km).

### 2.4 Evaluation of Surface Layer Schemes

The instrumented domain (Fig. 1a) was designed to study subgrid physical processes of NWP models. To this end, we aim to quantify errors introduced when using idealized SL schemes for complex terrain and to reveal how these errors vary with atmospheric conditions. One of the most popular SL schemes of the Weather Research and Forecasting (WRF) model (Skamarock et al. 2008) is WRF SL option 1 (Jiménez et al. 2012), which is an improved

version of the SL scheme introduced by Skamarock et al. (2008) and based on the fifth-generation Mesoscale Model (MM5) (Grell et al. 1995).

The physics formulation of WRF SL option 1 is based on Monin–Obukhov Similarity Theory (MOST), and it calculates the friction velocity according to Eq. 7:

$$u_* = \frac{kU}{\log\left(\frac{z}{z_0}\right) - \psi_m\left(\frac{z}{L}\right)}, \tag{7}$$

where $z$ is the height, $\kappa = 0.4$ is the von Kármán constant, $U$ is the wind speed at the lowest computational level, $z_0$ the roughness length, $z/L$ the stability, and $\psi_{m,h}$ the integrated Monin–Obukhov similarity function of momentum (or heat) defined according to Eq. 8,

$$\psi_{m,h}\left(\frac{z}{L}\right) = \int_0^{z/L} \left[1 - \phi_{m,h}(\xi)\right] \frac{d\xi}{\xi}, \tag{8}$$

where the dimensionless wind shear $\phi_m$ and potential temperature gradient $\phi_h$ are defined according to Eq. 9 and Eq. 10, respectively,

$$\phi_m\left(\frac{z}{L}\right) = \frac{\kappa z}{u_*} \frac{\partial U}{\partial z}, \tag{9}$$

and,

$$\phi_h\left(\frac{z}{L}\right) = \frac{\kappa z}{\theta_*} \frac{\partial \theta}{\partial z}, \tag{10}$$

with $\theta_*$ a temperature scale calculated with Eq. 11,

$$\theta_* = \frac{k(\theta_a - \theta_g)}{\log\left(\frac{z}{z_0}\right) - \psi_h\left(\frac{z}{L}\right)}, \tag{11}$$

where $\theta_a$ and $\theta_g$ the air and ground surface potential temperature, respectively.

In order to use Eq. 7 in a mesoscale model (i.e., WRF), $z_0$ is retrieved from the Land Surface Model (LSM), while the stability $z/L$ is calculated by the SL scheme; and in the case of WRF SL option 1 with Eq. 12,

$$\frac{z}{L} = \kappa \frac{g}{\theta_a} z \frac{\theta_*}{u_*^2}. \tag{12}$$

For more details on WRF SL option 1, see Jiménez et al. (2012).

Alternatively, in this study we implemented Monin–Obukhov (MO) equations to calculate time series of friction velocity for the period 27 August–26 September, 2016. This was preferred over running a complete WRF simulation in view of the difficulty of isolating the SL scheme from the LSM, and as it reduces uncertainties associated with inaccurate values of the roughness length, wind speed, and stability parameter, that were passed directly from the measurements and into the implemented MO equations solved by WRF SL option 1.

The roughness length $z_0$ was estimated using: (*i*) The combined wind speed measurements from the tower and the SODAR at site T1 and (*ii*) The three instrumented levels at towers T2 and T6 during periods with westerly winds and Neutral (N) conditions according to the classical methodology of Panofsky (1962). To reduce uncertainty of $z_0$, westerly winds were defined as being in the segment $270 \pm 5°$. As mentioned, (Sect. 2.3), N conditions were identified with $|L| > L_{TR}$, with $L_{TR} = 200$. For details on the velocity profiles used in

these calculations, see Figs. 17, 18, 19 in Appendix. The roughness length $z_0 = 0.013$ m so obtained was used to calculate the friction velocity according to Eq. 13:

$$u^*_{\text{sim}} = \frac{k\langle U\rangle}{\log\left(\frac{z}{z_0}\right) - \psi_m\left(\langle\frac{z}{L}\rangle\right)}. \tag{13}$$

Considering that many high-resolution simulations have grid-sizes ~ 1–3 km (Hong and Dudhia 2012), tests were conducted on the ability of the selected SL scheme to capture a friction velocity that agrees with the observed spatially averaged friction velocity. The friction velocity at $z = 10$ m was simulated, considering that all towers had instruments at that height and that the first level of NWP models is typically set to 10 m.

Given the dependence of $u_*$ on the local wind speed and stability (Eq. 7), these variables were spatially averaged for $z = 10$ m at all sites, as indicated by the brackets in Eq. 13.

## 3 Results

### 3.1 Stability Regimes

Typical ASL parameterizations diagnose the friction velocity and temperature fluxes in terms of the stability parameter $z/L$, but in reality, the latter is variable within a grid cell. To illustrate this variability, for the Aug 27 to Sep 26 period, we calculated the percentage of time the stability regimes Unstable (UN), Neutral (N), and Stable (S) occurred at each tower location. For each stability regime, the results were averaged across all towers, and consistent with Sect. 2.3, only periods with wind direction in the [westerly] sector 240°-290° are considered here and in Sects. 3.2 and 3.3.

As shown in Fig. 4, the UN, N, and S stability regimes were observed approximately 49 (49), 13 (15), and 37 (35) percent of the time, respectively. The parenthetical values are the percentages evaluated with the bulk Obukhov length ($L_{bulk}$) described in Sect. 2.3. The higher number of UN cases (49%) compared to S ones (37%) is due to the fact that winds in the sector 240°–290° are more frequently observed during daytime conditions for this season of the year.

The good agreement between the green and the brown bars in Fig. 4 suggests the overall stability of the instrumented region can be characterized with either $\langle L\rangle$ or $L_{bulk}$. The error

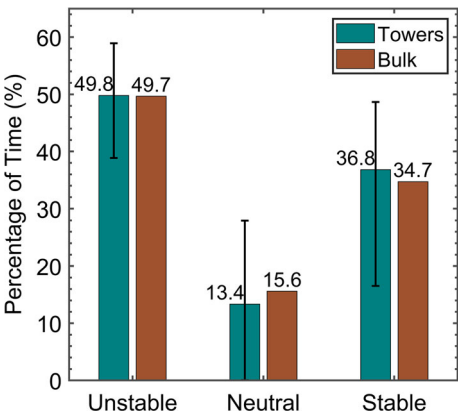


**Fig. 4** Percentage of time the stability regimes *UN*, *N,* and S were present during Aug 27 to Sep 26. Calculations were made for each tower, and the average across all towers is shown by teal-blue bar with the error bar indicating the maximum and minimum values. The brown bar corresponds to the distribution of stability regimes calculated using the 'Bulk Obukhov length' $L_{bulk}$ (Sect. 2.3)

bars in Fig. 4 are associated with the spatially averaged stability (green bars), and for each stability regime (UN, N and S), they indicate the maximum and minimum percentage of the time the same stability was observed at any of the towers.

To further interpret these results, Fig. 5a shows the percentage of time each stability regime was reported for all tower locations, where the blue, grey, and orange horizontal lines correspond to the percentage of time the UN, N, and S regimes assessed with $L_{bulk}$ were reported, respectively. The tower locations and terrain elevations corresponding with the data plotted in Fig. 5a are shown in Fig. 5b.

The higher spatial variability reported for the stable regime and indicated by the error bars in Fig. 4 was affected by the smaller number of stable cases at site T3. This site had an elevation of 405 m and it was located about 1 km north from site T2 (see Fig. 5b). At site T3, winds in the sector 240°–290° were less frequent than at other locations, and when they occurred, they were associated with higher values of friction velocity. In addition, at this site the range of variability of the Obukhov length was bigger than for the rest of the towers ( − 400 m to 400 m), and several cases with values of $L^* > 0$ fell in the neutral regime.

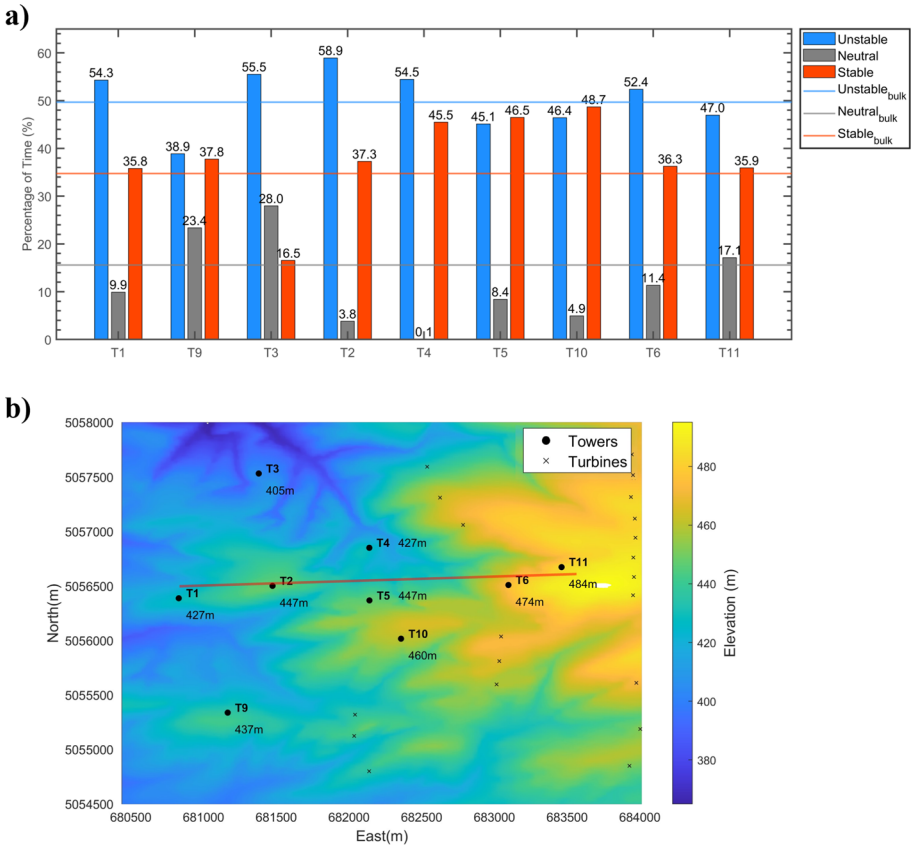


**Fig. 5 a** Percentage of time stability regimes were present at each tower location (T1 to T9) during Aug 27 to Sep 26. The color bar representation is in the inset. The horizontal lines of the same colors correspond to that based on *Bulk Obukhov length* for the same stability regimes. **b** Topography of instrumented region and tower's locations (same as Fig. 1)

On the other hand, the north–south transect of towers between sites T4, T5, and T10, and associated with terrain elevations of 427 m, 447 m, and 460 m, respectively, exhibited a higher number of stable cases. With regards to diagnosing stability in heterogeneous terrain, no clear correlation between the stability regimes and elevation was found.

Given the dependence of the Obukhov length on the friction velocity and temperature fluxes, we studied their spatial variability in Sects. 3.2 and 3.3.

### 3.2 Constant-Flux Layer

As mentioned in Sect. 1, the existence of a Constant-Flux Layer (CFL) is key to the SL parameterizations of NWP models. In this section, we used towers T1, T2, T6, and T11 (horizontal line in Fig. 5b) to study the CFL concept as a function of (i) stability regime, (ii) flux magnitude, and (iii) tower location. For doing so, the differences between $(\overline{u'w'})$ and $(\overline{w'T'})$ at $z = 3$ m and those at $z = 10$ m were calculated individually for T1, T2, T6, and T11. In this study, because of the small separation between levels (i.e., 7 m), the CFL approximation was taken to be valid when the differences between these two levels were less than 10%. Consistent with the study of Sfyri et al. (2018), momentum and temperature fluxes with absolute values smaller than 0.01 $m^2\ s^{-2}$ and 0.01 K m $s^{-1}$, respectively, were not included in the CFL analysis, as they are characterized by large random errors and affected by mesoscale trends (Sfyri et al. 2018; Klipp and Mahrt 2004).

To study the vertical variability of fluxes, values of $(\overline{u'w'})$ at $z = 3$ m are plotted against those at $z = 10$ m in Fig. 6a. Similarly, values of $(\overline{w'T'})$ at $z = 3$ m are plotted against those at $z = 10$ m in Fig. 6b. These plots were calculated for all tower sites (T1, T2, T6, and T11) and for each stability regime (UN, N, and S). On Figs. 6a–b, lines with slopes 1, 0.9, and 1.1 are plotted, and all points located in the area bounded by slope = 0.9 and 1.1 lines were assumed to satisfy the CFL approximation.

#### 3.2.1 Fluxes Vertical Variability

**Longitudinal Momentum Flux $(\overline{u'w'})$** As seen in Fig. 6a, the differences in the longitudinal momentum flux $(\overline{u'w'})$ were more affected by the stability regimes (UN, N, or S) than by the towers' locations, except for site T11, where the differences between levels and the scatter in the data were the highest of all sites. In general, for the UN regime, $\overline{u'w'}$ varied in the interval [-0.6, 0] $m^2\ s^{-2}$, and the median $\overline{u'w'}$ was about $-0.2\ m^2\ s^{-2}$. In addition, a bigger range of variability was reported at site T11, where the values of $\overline{u'w'}$ at $z = 3$ m were systematically higher than 10% of those at $z = 10$ m, e.g., see the high number of points above slope = 0.9 line in Fig. 6a.

As discussed earlier, neutral conditions (as defined in Table 2) were infrequently reported, and at sites T1, T2, T6, and T11, they were only present ~ 5–17% of the time (see Fig. 5a). For the N regime, $\overline{u'w'}$ varied between $[-0.5,\ -0.1]\ m^2\ s^{-2}$, the median $\overline{u'w'}$ was about $-0.3\ m^2\ s^{-2}$, and most measurements were associated with values of $L^* < 0$. The scatter of the data as well as the differences between levels were smaller than for the UN regime, likely due to the higher signal-to-noise ratio in $\overline{u'w'}$ measurements during high wind speed periods. For the S regime, $\overline{u'w'}$ varied in the interval $[-0.4, 0]\ m^2\ s^{-2}$, and the median $\overline{u'w'}$ was about $-0.1\ m^2\ s^{-2}$. For this regime, the scatter of $\overline{u'w'}$ between levels was smaller than for the UN regime, which was expected locally, as wind speed and flux magnitude tend to be

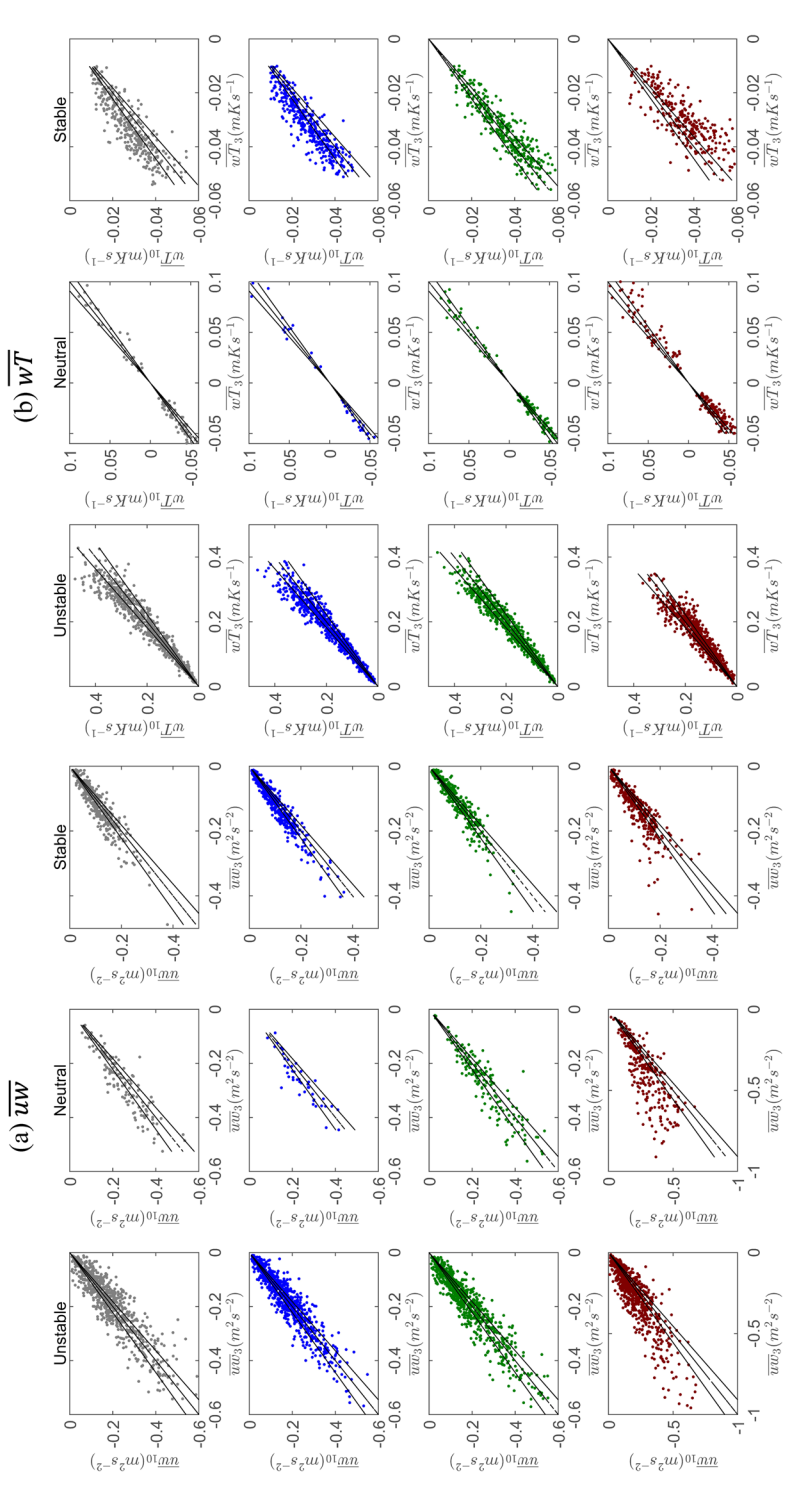


**Fig. 6** **a** Scatter plots of longitudinal momentum flux ($\overline{u'w'}$) at z = 3 m (x-axis) versus longitudinal momentum flux ($\overline{u'w'}$) at z = 10 m (y-axis); **b** Same as in (**a**) but for the temperature flux ($\overline{w'T'}$). The columns correspond to UN, N, and S regimes (from left to right), and the rows to towers T1 (gray), T2 (blue), T6 (green), and T11 (maroon)

smaller for stable periods (Stull 1988; Pope 2000). On the other hand, we expected to find smaller differences between sites for the UN regime, as the role of terrain heterogeneities should have been attenuated by the bigger eddy size and enhanced mixing during convective conditions, however, percentual differences between sites were comparable between the UN and S regimes.

**Temperature Flux ($\overline{w'T'}$)** The variability of $\overline{w'T'}$ was also more affected by the stability regimes (UN, N, or S) than by the towers' locations. For the UN regime, the temperature flux ($\overline{w'T'}$) varied in the interval [0, 0.4] $Kms^{-1}$, and the median $\overline{w'T'}$ was about 0.16 $Kms^{-1}$. In addition, $\overline{w'T'}$ measurements were symmetrically distributed with respect to slope $= 1$ lines, and the differences between levels and scatter in the data were smaller than for $\overline{u'w'}$, nonetheless, as we expected, the variability of the temperature flux was more complex than for the momentum flux. For the N regime, a narrow range of variability for $\overline{w'T'}$ between [$-0.05, 0.1$] $Kms^{-1}$ was observed for all the sites. Moreover, the scatter between levels was the smallest of all stability regimes. Nonetheless, a high number of points did not satisfy the CFL, likely due to the small magnitude of the fluxes, and also a higher number of points did not satisfy our quality control requirements when compared with the momentum flux ($\overline{u'w'}$), i.e., the absolute values of $\overline{w'T'}$ were $< 0.01$ $Kms^{-1}$, and/or the fluxes at levels $z =$ 3 m and $z = 10$ m exhibited different signs. For the S regime, $\overline{w'T'}$ varied in the interval [$-$ 0.05, 0] $Kms^{-1}$, and both the scatter between levels and the differences between sites were higher than for the UN regime. For example, for the westernmost sites, i.e., T1 and T2, values of $\overline{w'T'}$ at $z = 10$ m were systematically lower than those at $z = 3$ m. e.g., see how the distribution of points is skewed with respect to slope $= 1$ lines in Fig. 6b. On the other hand, at sites T6 and T11, located about 1.6 and 2 kms east from site T2, respectively, the terrain elevation was ~ 30 to 40 m higher than at T2, and $\overline{w'T'}$ values at $z = 10$ m were frequently higher than those at $z = 3$ m, especially at site T11. Site T11 was located ~ 200 m north from the transect between towers T1, T2, and T6, and local heterogeneities and enhanced surface roughness due to the presence of wheat crops could have affected the measurements.

### 3.2.2 Constant-Flux Layer Validity

Because the number of UN, N, and S cases were not constant across sites (as shown in Fig. 5a), for each tower site (T1, T2, T6, and T11) and stability regime (UN, N, and S), the CFL validity was calculated as the ratio between the total number of points located in the area bounded by slopes $= 1.1$ and 0.9 lines in Fig. 6a–b (for the momentum ($\overline{u'w'}$) and temperature ($\overline{w'T'}$) flux, respectively), and the total number of records (addition of UN, N, and S cases), where the latter was the same for all towers and corresponded to the total number of westerly records discussed in Sect. 3.1.

The CFL validity results (expressed in % of time) for the momentum flux ($\overline{u'w'}$), the temperature flux ($\overline{w'T'}$), and both momentum and temperature fluxes ($\overline{u'w'}$ and $\overline{w'T'}$) simultaneously are shown in Fig. 7a–c, respectively.

The CFL validity for $\overline{u'w'}$ and $\overline{w'T'}$ was higher for the UN regime. Nonetheless, the CFL validity for $\overline{u'w'}$ was only ~ 20% at T1, T2, and T6, and ~ 10% at T11. While the CFL validity for $\overline{w'T'}$ was only ~ 30% at T1, T2, and T6, and ~ 10% at T11. For the S regime, the CFL validity for $\overline{u'w'}$ was ~ 10%, while the CFL validity for $\overline{w'T'}$ exhibited slightly higher variability across the sites, i.e., between 8–13% at T1, T2, and T6, and 5% at T11.

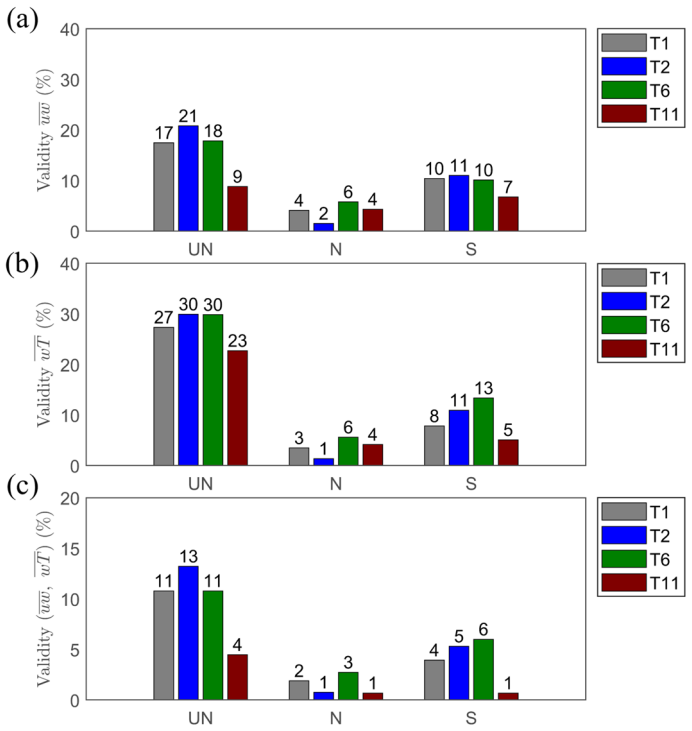


**Fig. 7** **a** CFLValidity (in % of time) for the momentum flux ($\overline{u'w'}$), **b** temperature flux ($\overline{w'T'}$), and **c** momentum and temperature flux simultaneously ($\overline{u'w'}$, $\overline{w'T'}$). The results were calculated for each stability regime (UN, N, and S), and for each tower location (T1, T2, T6, and T11

For the N regime, the CFL was satisfied between 1 and 6% of the time, and no important differences between towers were observed. Note that this regime was highly infrequent compared to the UN or the S regime. For completeness, as indicated in Fig. 7c, the percentage of cases that simultaneously satisfied the CFL for $\overline{u'w'}$ and $\overline{w'T'}$ were < 13% for the UN regime, < 3% for the N regime, and between 1–6% for the S regime. Thus, the data suggests the CFL generally does not hold, not even at small horizontal and vertical scales such as the ones explored in this experiment.

### 3.3 Fluxes Horizontal Variability

To study the horizontal variability of fluxes, local values of $\overline{u'w'}$ are plotted against $\langle\overline{u'w'}\rangle$ (spatial-averaging across towers T1, T2, T6, and T11) in Fig. 8a. Similarly, $\overline{w'T'}$ from the tower sites against $\langle\overline{w'T'}\rangle$ are shown in Fig. 8b. The plots were done for each stability regime (UN, N, and S), and they seek to quantify the differences between local turbulent fluxes and their spatially averaged counterparts.

As in Sect. 3.2, in Fig. 8a–b, lines with slopes 1, 0.9, and 1.1 are plotted. The results were similar to the ones associated with the CFL in Sect. 3.2.

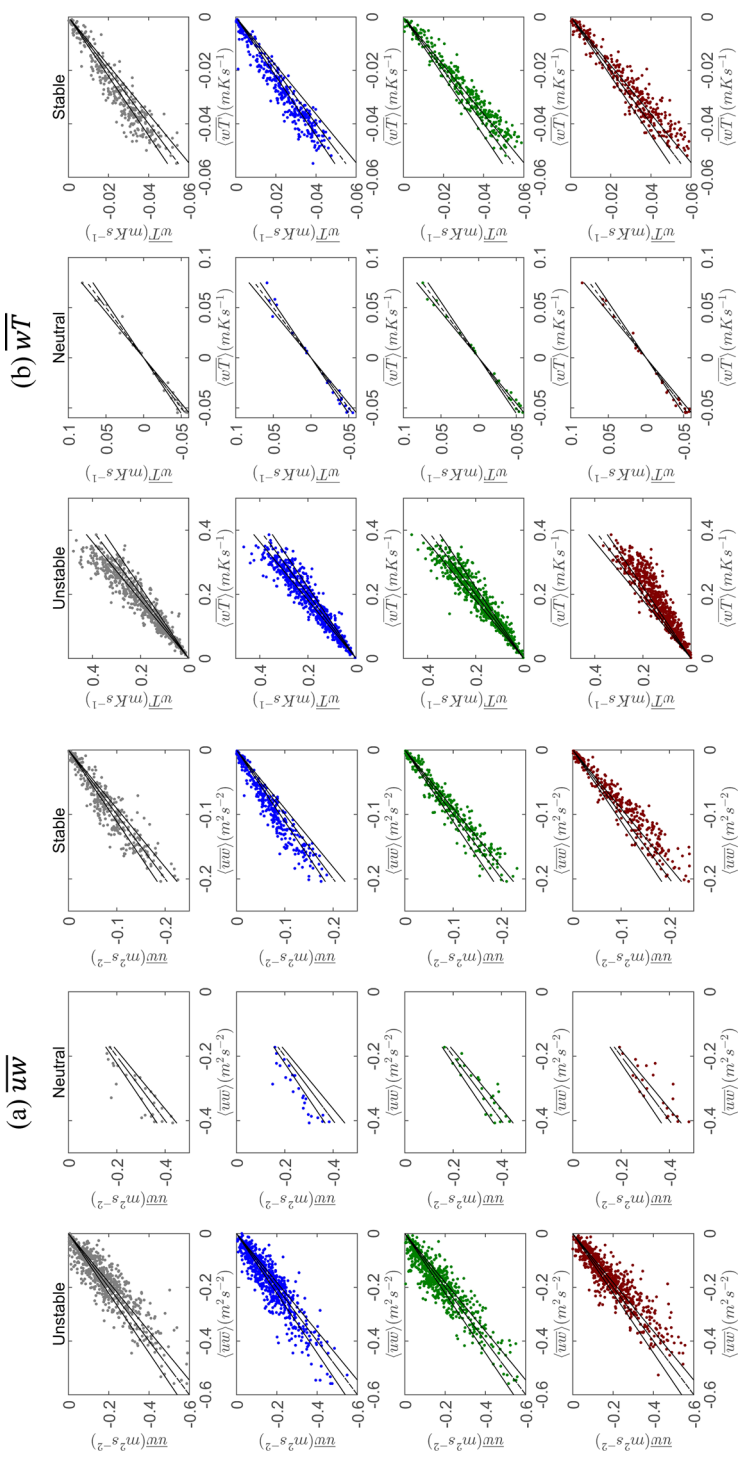


**Fig. 8 a** Scatter plots of $\overline{(u'w')}$ at z = 10 m (y-axis) versus its spatially averaged value $\langle \overline{u'w'} \rangle$ at the same height (x-axis) at a given time; **b** Same as in (**a**) but for $\overline{(w'T')}$ at z = 10 m (y-axis). The columns correspond to UN, N, and S (from left to right), and the rows to towers T1 (gray), T2 (blue), T6 (green), and T11 (maroon)

### 3.3.1 Unstable (UN)

This regime exhibited the highest deviations between the local and spatially averaged momentum flux, $\overline{u'w'}$ and $\langle\overline{u'w'}\rangle$, respectively. At all sites, deviations > 10% were observed. At T1, T2, and T6, data points were symmetrically distributed with respect to slope = 1 lines (Fig. 8a). In contrast, at T11, values of $\overline{u'w'}$ were higher than $\langle\overline{u'w'}\rangle$ most of the time. For this stability, the similarity between the horizontal variability of $\overline{u'w'}$ and the CFL efficacy of the latter is remarkable.

On the other hand, this regime aso exhibited the highest deviations between the local and spatially averaged temperature flux, $\overline{w'T'}$ and $\langle\overline{w'T'}\rangle$, respectively. At all sites, deviations > 10% were frequently observed. At all sites (except for T11), data points were symmetrically distributed with respect to slope = 1 lines (Fig. 8b) and the horizontal variability of $\overline{w'T'}$ was less than for $\overline{u'w'}$ for this stability, analogous to the CFL results for $\overline{w'T'}$ in Sect. 3.2.

### 3.3.2 Neutral (N)

For all sites, deviations between the local and spatially averaged momentum flux were < 10% most of the time, and the horizontal variability of $\overline{u'w'}$ was the lowest of all stability regimes. Nonetheless, the distribution of points with respect to slope = 1 lines presented more site-to-site variability when compared to the CFL results of Sect. 3.2 ($\overline{u'w'}$—N), i.e. values of $\overline{u'w'}$ at T2 had less scatter than other sites and were systematically lower than the spatially averaged flux $\langle\overline{u'w'}\rangle$. At T11, differences between local and spatially averaged values at $z = 10$ m were about the same than those observed at T1, T2, and T6 (as opposed to the CFL results reported in Sect. 3.2). This suggests that the least agreement with the CFL concept for N conditions at T11 was a result of anomalously high values of $\overline{u'w'}$ at $z = 3$ m (Fig. 5a). Nonetheless, is important to notice that the number of N points were lesser than in Sect. 3.2, a consequence of requiring N conditions to be simultaneously satisfied at sites T1, T2, T6, and T11.

On the other hand, for all sites, deviations between the local and spatially averaged temperature flux were < 10% most of the time, and the scatter of the data for $\overline{w'T'}$ was less than for $\overline{u'w'}$ during N conditions (Fig. 8a–b). These results were analogous to the ones in Sect. 3.2 ($\overline{w'T'}$-N).

### 3.3.3 Stable (S)

The scatter between local and spatially averaged momentum flux was lower than for the UN regime, and the differences between sites more evident. This is analogous to what we observed in Sect. 3.2 ($\overline{u'w'}$—S). For this regime, $\overline{u'w'}$ differences between sites were higher than the differences between levels (for fixed sites), as evidenced by the different distributions of points with respect to slope = 1 lines for sites T1, T2, T6, and T11 shown in Fig. 8a. More interestingly, the magnitude of the flux did not affect the differences between local values of $\overline{u'w'}$ and the spatially averaged flux $\langle\overline{u'w'}\rangle$, which was analogous to what we observed for the CFL results in Sect. 3.2 ($\overline{u'w'}$—S).

On the other hand, the scatter between the local and spatially averaged temperature flux was lower than for the UN regime, and deviations higher than 10% were frequently observed

at all sites. In addition, the differences between sites were the highest of all stability regimes, similarly to what we observed for $\overline{u'w'}$.

### 3.4 Surface-Layer Parameterizations

We calculated time series of the simulated and observed (spatially averaged across all 9 towers) friction velocity for the period 27 August–26 September, 2016. The time series of simulated (blue) and observed (black) friction velocity are shown in Fig. 9a, and the difference between them is the error calculated according to Eq. 14 and indicated in Fig. 9b (left *y* axis):

$$\text{Error}\left(ms^{-1}\right) = u^*_{\text{sim}} - \langle u^* \rangle, \tag{14}$$

with $u^*_{\text{sim}}$ and $\langle u^* \rangle$, the simulated and spatially averaged observed friction velocity described in Sect. 2.4 and calculated with Eq. 13 and Eq. 6, respectively. The error (Eq. 14) expressed as a percentage of the observed friction velocity is the percentual error calculated with Eq. 15 and indicated in Fig. 9b (right *y* axis):

$$\text{Error}(\%) = \frac{\text{Error}}{\langle u^* \rangle} \cdot 100. \tag{15}$$

To effectively study the skill of the SL scheme for the period between 27 August and 26 September 2016, the data plotted in Fig. 9b–c were used to calculate error, wind speed,

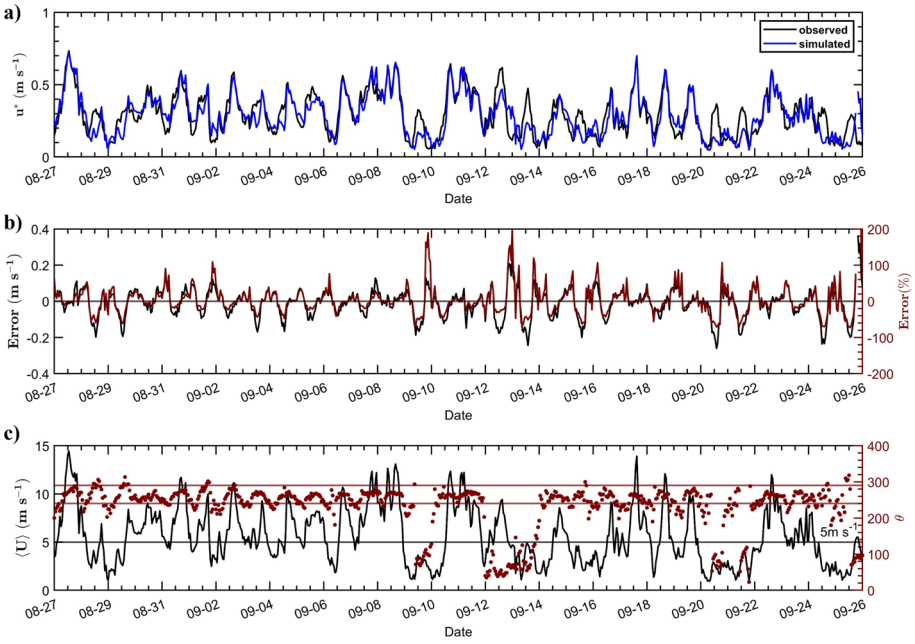


**Fig. 9** **a** Time series of friction velocity for 27 August–26 September 2016. The black line is the spatially averaged friction velocity $\langle u^* \rangle$ measured by all towers at z = 10 m, and the simulated friction velocity at z = 10 m is in blue; **b** Time series of the Error between the two-time series of **a** in m $s^{-1}$ (left *y* axis) and in percentage (right *y* axis); **c** Time series of the observed spatially-averaged wind speed (black line) and wind direction (maroon line) with the black line indicating the 5 m $s^{-1}$ threshold and the maroon lines demarcating the westerly wind regime between 240° and 290°

and wind direction colormaps, as shown in Fig. 10a–c, respectively. In Fig. 10a–c, the rows corresponds to different days, while the columns corresponds to different hours (in Pacific Standard Time). Since the relationship between the skill of the SL scheme and the current meteorological conditions was of interest, we adopted the wind-regime classification used by Fernando et al. (2015) for their complex terrain observations: Quiescent (wind speeds between 0 and 5 m $s^{-1}$), *Transitional* (wind speeds between 5 and 10 m $s^{-1}$), and *Synoptic* (wind speeds higher than 10 m $s^{-1}$), with the difference being that we used the observed winds at $z = 10$ m instead of the 700-hPa winds. In this classification, *Transitional* flows are associated with rapidly changing winds and turbulence levels, such as the ones observed during the morning and evening transition periods, while *Synoptic* flows are associated with synoptic winds higher than 10 m $s^{-1}$ (Fernando 2010).

As shown in Fig. 9b, errors between -0.1 to 0.1 m $s^{-1}$ were observed most of the time, which when normalized by the observed friction velocity, corresponds to -40 to 85% errors. The.friction velocity was frequently underpredicted by the SL scheme during the day and overpredicted at night, when high percentual errors were reported (see Fig. 9a–b). For the nominally observed westerly winds (maroon lines in Fig. 9c) with speeds > 5 m $s^{-1}$ (black horizontal line in Fig. 9c), the implemented SL scheme captured the diurnal variability of friction velocity well (Fig. 9a–b).

For example, on 27 August, westerly winds > 5 m $s^{-1}$ were present most of the day, and the simulated friction velocity was almost identical to the observations between 07:00–16:00 LT (local time) (Figs. 9a, 10a–c). For this day, the Mean Absolute Error (MAE) was about 9% of the observed friction velocity (daily averaged). Similar cases were observed on 06, 17, and 19 September, all associated with westerly winds with speeds > 5 m $s^{-1}$ and MAEs between 8 and 16% of the observed friction velocity (Figs. 9c, 10b, c).

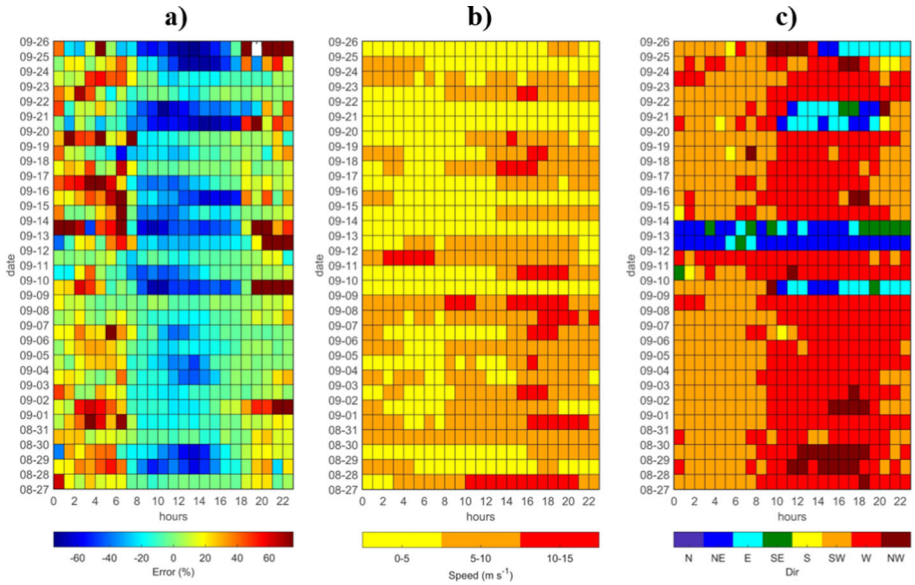


**Fig. 10** Color maps of **a** 1 h Error (%) between simulated and observed friction velocities; **b** 1 h wind speed regimes; and **c** 1 h wind direction regime for the period 27 August 2016 to 26 September 2016. The abscissa indicates the local time whereas the ordinate is the date

For the rest of the days, the SL scheme was able to capture the time variability trend of friction velocity over a diurnal cycle, but not the exact value. This was expected given the heterogeneous nature of the terrain and the wide range of meteorological phenomena that characterizes the region (Wilczak et al. 2019). In fact, errors as high as 60% of the observed friction velocity were present on most days at night when the friction velocity was less than about 0.2 m $s^{-1}$ (for more details see Fig. 20).

The study period spanned diverse meteorological regimes. For instance, cases with predominantly westerly winds with both quiescent and transitional regimes were observed (i.e. 03, 04 September). For the rest of the westerly-flow days, particularly during quiescent winds, the flow exhibited a characteristic diurnal variability with a northerly/northwesterly component (NW) during daytime and a southerly/southwesterly component (SW) during nighttime (e.g., 28, 29 August and 24 September).

Cases with easterly winds with quiescent and transitional regimes were also observed, but they were not analyzed as they might be contaminated by wake effects of an array of turbines located east of the towers (Fig. 1a). Also recall that the roughness length used in simulations ($z_0 = 0.013$ m) corresponded to westerly winds.

The degree of subgrid variability associated with the observed errors at NWP-model resolution for selected days was also investigated. The subgrid variability was assessed through the Mean Absolute Deviation (MAD) calculated according to Eq. 16:

$$\mathrm{MAD} = \frac{1}{N}\sum_{i=1}^{N}\left|u^*_{\mathrm{obs}}(x_i, t) - \langle u^*_{\mathrm{obs}}\rangle\right|. \tag{16}$$

A high temporal correlation between the Error and the spatial heterogeneity of the flow, quantified through the Mean Absolute Deviation (MAD), was noted, as discussed below.

From all westerly-flow days in the period Aug 27 and September 26, 2016, we identified the ones associated with the highest and the lowest SL scheme errors, which are indicated in Tables 3, 4, respectively. These errors were quantified by the MAE, calculated for (i) A 24-h period (denoted by $\mathrm{MAE_{day}}$ in Tables 3, 4), and (ii) between 12:00 and 14:00 LT (denoted by $\mathrm{MAE_{sub}}$ in Tables 3, 4). ($\mathrm{MAE_{day}}$) and ($\mathrm{MAE_{sub}}$) expressed as a percentage of the temporally averaged observed friction velocity are denoted by $\mathrm{Error_{day}}$ and $\mathrm{Error_{sub}}$ in Tables 3, 4.

For the list of days in Table 3 (associated with the poorest performance of the SL scheme),positive errors of about 0.1 m $s^{-1}$ were frequently observed at night, while variable

**Table 3** Days associated with the highest SL scheme errors for 27 August 2016 to 26 September 2016

| Date | $\mathrm{MAE_{day}}$ (m $s^{-1}$) | $\mathrm{Error_{day}}$ (%) | $\mathrm{MAE_{sub}}$ (m $s^{-1}$) | $\mathrm{Error_{sub}}$ (%) | Wind Dir | Speed range (m $s^{-1}$) | Wind regime |
|---|---|---|---|---|---|---|---|
| 08/28/16 | 0.08 | 32.8 | 0.17 | 52.7 | NW | 5–10 | Q, T |
| 08/29/16 | 0.06 | 26.6 | 0.18 | 57.3 | NW | < 5 | Q |
| 09/03/16 | 0.05 | 17.6 | 0.15 | 40.7 | W | 5–10 | Q, T |
| 09/04/16 | 0.04 | 14 | 0.13 | 38.1 | W | 5–10 | Q, T |
| 09/15/16 | 0.08 | 38 | 0.16 | 52 | W | < 5 | Q |
| 09/24/16 | 0.08 | 35.4 | 0.23 | 69.9 | W, SW | < 5 | Q |

The Mean Absolute Error (MAE) and the percentual error (Error) were calculated daily ($\mathrm{MAE_{day}}$ and $\mathrm{Error_{day}}$) and between 12:00 and 14:00 LT ($\mathrm{MAE_{sub}}$ and $\mathrm{Error_{sub}}$). These metrics and their associated wind regimes are indicated for the list of days shown below

**Table 4** Analogous to Table 3, but for selected days with the lowest SL scheme errors for 27 August 2016 to 26 September 2016

| Date | $MAE_{day}$ (m $s^{-1}$) | $Error_{day}$ (%) | $MAE_{sub}$ (m $s^{-1}$) | $Error_{sub}$ (%) | Wind Dir | Speed range (m $s^{-1}$) | Wind regime |
|---|---|---|---|---|---|---|---|
| 08/27/16 | 0.04 | 8.5 | 0.01 | 1.1 | W | 5–15 | T |
| 09/06/16 | 0.04 | 12.6 | 0.07 | 24.9 | W | 2–11 | Q, T |
| 09/17/16 | 0.03 | 8 | 0.01 | 1 | W | 4–15 | Q, T |
| 09/19/16 | 0.04 | 15.5 | 0.02 | 5.1 | W | 4–10 | Q, T |

negative errors as high as 0.2 m $s^{-1}$ were observed during the day (Fig. 11a–b). The impact of these errors on the skill of the SL scheme depends on the magnitude of the friction velocity. For instance, 1-h (positive) and (negative) errors between (30–106%) and of about (60%) of the observed friction velocity were reported.

For the six cases in Table 3: 28, 29 August, and 03, 04, 15, and 24 September, the parameterization scheme was challenged during 08:00–18:00 LT (Fig. 11a–b), and the winds were approximately westerly, as indicated by the two horizontal lines in Fig. 11d.

The error defined in Eq. 14 increased monotonically (in magnitude) between 08:00 LT until about 12:00–14:00 LT when it peaked, and then it decreased monotonically until 18:00 LT (Fig. 11b). For most days, the highest errors were associated with quiescent winds between 08:00 and 14:00 LT. However, on 28, 29 August and 3, 4 September, the errors between 14:00 and 18:00 LT were smaller than the errors on 15, 24 September, likely in part due to the presence of transitional winds for the latter days (between 5 and 10 m $s^{-1}$) (Fig. 11c).

As indicated in Table 3, the Mean Absolute Error (MAE) between 12:00 and 14:00 LT (when errors peaked) ($MAE_{sub}$) was about an order of magnitude higher than the daily MAE ($MAE_{day}$). Values of ($MAE_{day}$) and ($MAE_{sub}$) expressed as a percentage of the observed friction velocity are denoted by ($Error_{day}$) and ($Error_{sub}$) in Table 3, respectively. $Error_{day}$ varied between 18 and 38% for most days, while $Error_{sub}$ varied between 38 and 70%. In general, the percentual error between 12:00 and 14:00 LT ($Error_{sub}$) was about two times higher than the daily percentual error ($Error_{day}$), thus suggesting the skill of SL schemes in complex terrain is more sensitive to prediction errors during the day (as previously observed in Fig. 11a).

As shown in Fig. 11e, for all selected days, the MAD followed the simulation error between 08:00 and 18:00 LT (Fig. 11b), suggesting that subgrid variability might be a good predictor for errors when 1–3 km horizontal resolution is used in NWP models.

Further, the time evolution of the error and MAD over the diurnal cycle for 03 September and shown in Fig. 12a suggests that during 08:00–18:00 LT, the Error and MAD peaked around 12:00–14:00 LT, consistent with previous observations (Fig. 11a), and the SL scheme under-predicted the spatially averaged friction velocity. Moreover, the parameterization scheme under-predicted the observed friction velocity at T1, T2, T6, and T11 (east–west transect) and deviated from the spatially averaged friction velocity (Fig. 12b), consistent with the increasing trend of MAD.

For completeness, the time series in Fig. 11a–e were recalculated for the days indicated in Table 4 and are shown in Fig. 13a–e. These days had the lowest errors for the entire observational period, as signified by $Error_{day}$ between 8 and 16% in Table 4. In contrast to what we observed for the list of days in Table 3 (Fig. 11a), the simulated friction velocity

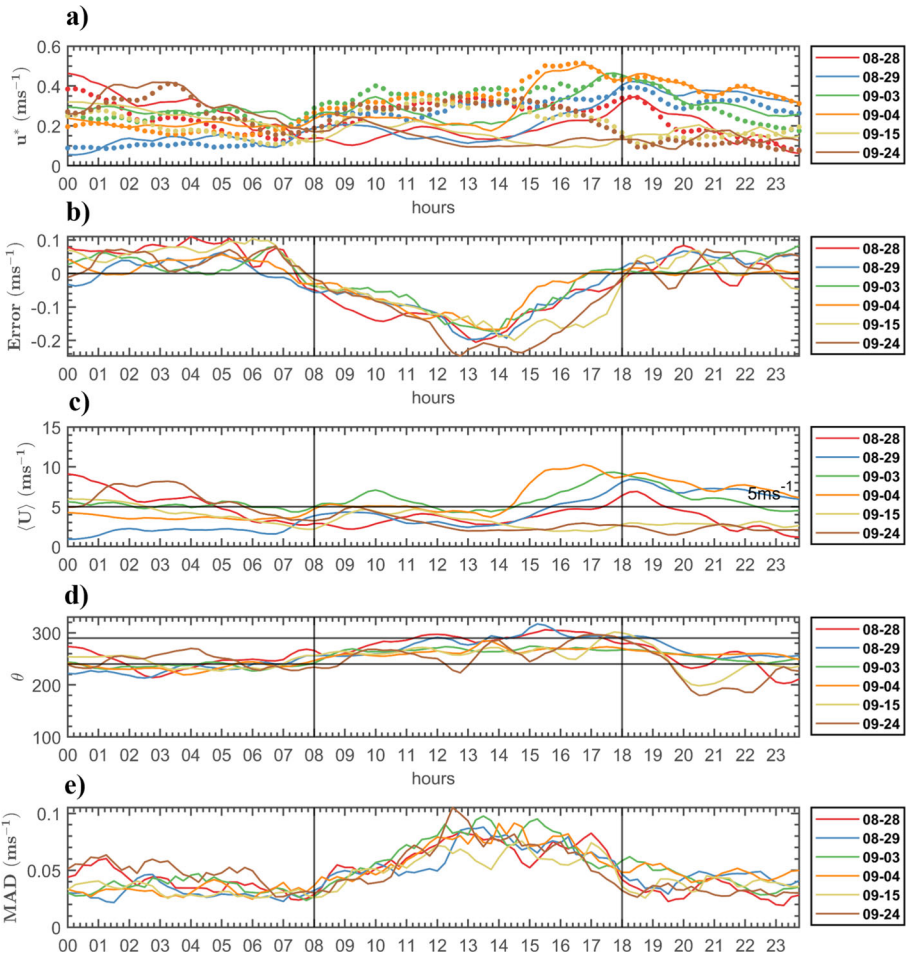


**Fig. 11** 24-h time series of **a** Observed (dots) and simulated (solid lines) friction velocity; **b** Error; **c** Observed wind speed; **d** Wind direction ($\theta$); and **e** Mean Absolute Deviation (MAD) of friction velocity at z = 10 m calculated using all the towers. The selected days 08/28/16, 08/29/16, 09/03/16, 09/04/16, 09/15/16, and 09/24/16 are indicated by different colors. The abscissa in **a**–**e** is the hour of the day in local time

was remarkably closer to the observations and no distinct performance trends were observed for the SL scheme over a diurnal cycle (Fig. 13a). This was supported by values of $MAE_{sub}$ and $MAE_{day}$ of the same order of magnitude, as indicated in Table 4. Nonetheless, positive (negative) errors were frequently observed at night (day) for the days in Table 4.

Westerly winds with speeds > 5 m $s^{-1}$ were frequently observed (Fig. 13c–d), likely responsible for the higher values of friction velocity and thus the higher overall skill of the SL scheme for these days (Fig. 13a), as evidenced by the good agreement between the observed wind speed and friction velocity for all days between 08:00 and 18:00 LT (Fig. 13a, c).

As shown in Fig. 13e, the spatial heterogeneity of the flow quantified by MAD did not exhibit a distinct variability over a diurnal cycle (as opposed to Fig. 11e). Similarly to what we observed earlier (Fig. 11b, e), the MAD had an influence on the simulation error for the days in Table 4, as evidenced by the temporal correlation between the two time series in

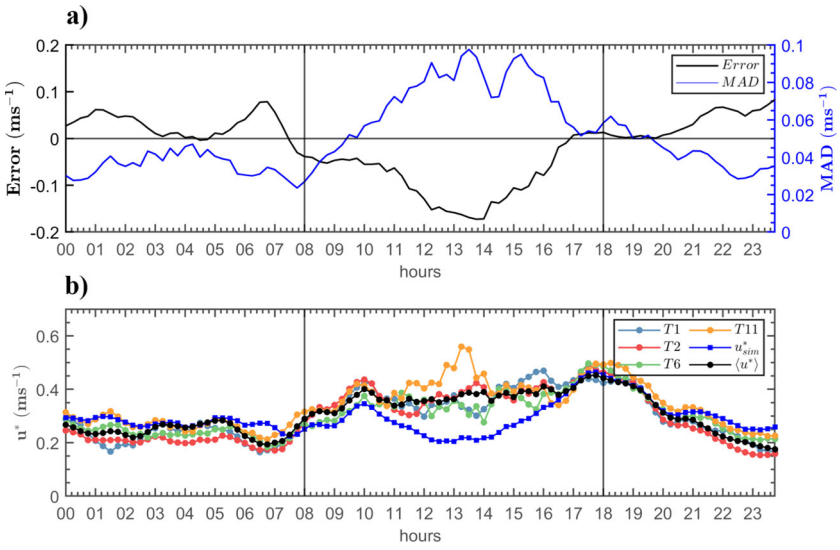


**Fig. 12** 24-h time-series for 03 September 2016. **a** Error (black line with values on the left ordinate) and MAD (blue line, right ordinate); and **b** Observed friction velocity at T1, T2, T6 and T11 compared with the spatially averaged observed $\langle u^* \rangle$ (blue line with markers) and simulated friction velocity $u^*$(black line with markers). The abscissa in **a**-**b** is the hour of the day in local time

Fig. 13b, e. For these days, the magnitude of the MAD was approximately the same than for days with the highest SL scheme errors indicated in Table 3 (Figs. 11e; 13e). However, the efficacy of the MAD to diagnose SL scheme errors for these days was lower.

Figure 14 a-b are the analogues of Fig. 12a–b, but for 06 September, which is representative of the days indicated in Table 4. The contrast between Figs. 12 and 14 is remarkable. It is not clear why the MAD correlates so well with the simulation error for the days when the skill of the SL scheme was the poorest (Table 3), and this correlation dropped for days where the skill of the SL scheme was the highest (Table 4), even though similar MAD values between -0.1 to 0.1 m s$^{-1}$ were present in both cases.

The percentual differences between local and spatially averaged values of $u^*$ at $z = 10$ m for unstable conditions between 12:00 and 15:00 PST for the entire observational period 27 August to 26 September 2016 are shown together with the instrumented region's elevation in Fig. 15a. Figure 15b is analogous to Fig. 15a, but for Stable conditions between 00:00 and 03:00 PST.

In general, spatial differences (in %) in $u^*$ across sites were not very different between the UN and S regimes, and no clear correlations between terrain elevation and deviations between local and spatially averaged friction velocity were present, likely due to the gentle nature of the terrain (e.g., see the difference in horizontal and vertical scales in Fig. 1a), the lack of measurements in low-laying areas (except for T3), and the higher frequency of wind speeds > 5 m s$^{-1}$ for the selected westerly winds. Nonetheless, at individual locations, deviations between $u^*$ and $\langle u^* \rangle$ were more affected by the stability regime (UN or S), e.g., at sites T1 and T5, these deviations remained approximately constant as the stability regime changed, whereas big differences were observed at sites T2, T6, and T11, where the proximity to local ridges could have had an influence. In addition, for the UN regime, $u^*$ values were only ~ 2% higher than $\langle u^* \rangle$ at site T3, and ~ 22% higher at T9. Conversely, for the S regime, $u^*$ values were ~ 33% higher than $\langle u^* \rangle$ at site T3, and ~ 2% higher than $\langle u^* \rangle$ at T9. The extent

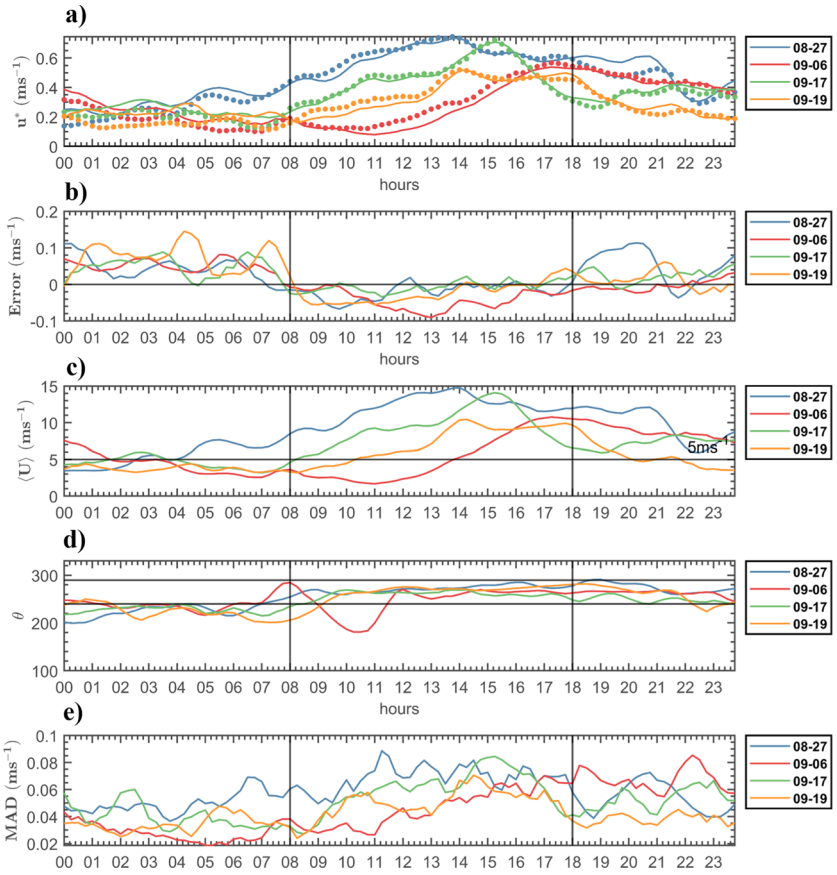


**Fig. 13** 24-h time series of **a** Observed (dots) and simulated $u^*_{sim}$ (solid lines) friction velocity; **b** Error; **c** Observed wind speed; **d** Wind direction ($\theta$); and **e** Mean Absolute Deviation (*MAD*) of friction velocity at z = 10 m calculated using all towers for 08/27/16, 09/06/16, 09/17/16, and 09/19/16. The abscissa in (**a**–**e**) is the hour of the day in local time

to which the terrain contributed to these alternating phenomena was beyond the scope of this work and would likely require space-resolved instrumentation (e.g., scanning lidars), or high-resolution Large Eddy Simulations (LES). For completeness, we calculated the analogous of Fig. 15a–b, but for the deviations between $\overline{wT}$ and $\langle\overline{wT}\rangle$ (for details see Fig. 21). For $\overline{wT}$, the overall heterogeneity between the UN and S regimes was similar, but the spatial variability between towers (in %) was higher and more complex than the one observed for the friction velocity.

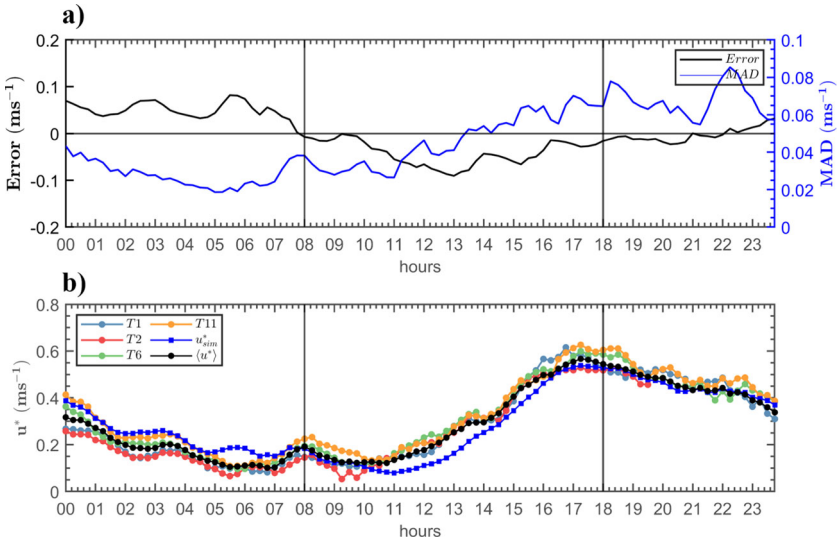


**Fig. 14** 24-h time-series for 06 September 2016. **a** Error (black line with values on the left ordinate) and *MAD* (blue line, right ordinate); and **b** Observed friction velocity at T1, T2, T6, and T11 compared with the spatially averaged observed $\langle u^* \rangle$ (blue line with markers) and simulated friction velocity $u^*_{sim}$ (black line with markers). The abscissa in (**a–b**) is the hour of the day in local time

## 4 Discussion

### 4.1 CFL Validity

For UN conditions, CFL for $\overline{u'w'}$ was satisfied about 10–20% of the time, and CFL for $\overline{w'T'}$ was satisfied about 20–30% of the time. For this stability regime, differences in CFL validity across sites were the highest, and the high local deviations observed between levels at site T11 were likely due to local terrain heterogeneities. For the S regime, CFL for $\overline{u'w'}$ was satisfied about 10% of the time, and CFL for $\overline{w'T'}$ was satisfied about 5–13% of the time, with higher differences between sites when compared to $\overline{u'w'}$. For N conditions, CFL for both $\overline{u'w'}$ and $\overline{w'T'}$ was satisfied $< 5\%$ of the time, mostly a consequence of the small number of N cases. Interestingly, for $\overline{u'w'}$, differences in CFL validity across sites were the highest for UN conditions, while for $\overline{w'T'}$, differences in CFL validity across sites were the highest for the S regime.

Our results have both differences and similarities with previous studies, which are most likely due to different [largely unknown] interactions between local terrain and background flow/stability. For example, Sfyri et al. (2018) found that for unstable and stable conditions, the CFL condition is satisfied about 1% of the time for the momentum fluxes and about 50% of the time for temperature fluxes. Nadeau et al. (2013) found that in the first 6 m above a steep slope (30°–40°) in the Swiss Alps, fluxes can be more than an order of magnitude different from their ground values. Our study, however, is more detailed than the previous ones as it investigated the validity of CFL using multiple towers over a small horizontal extent (1–3 km) within a mesoscale grid cell. In addition, we found that by choosing a sufficiently thin vertical layer (i.e., 7 m), small variability can be observed.

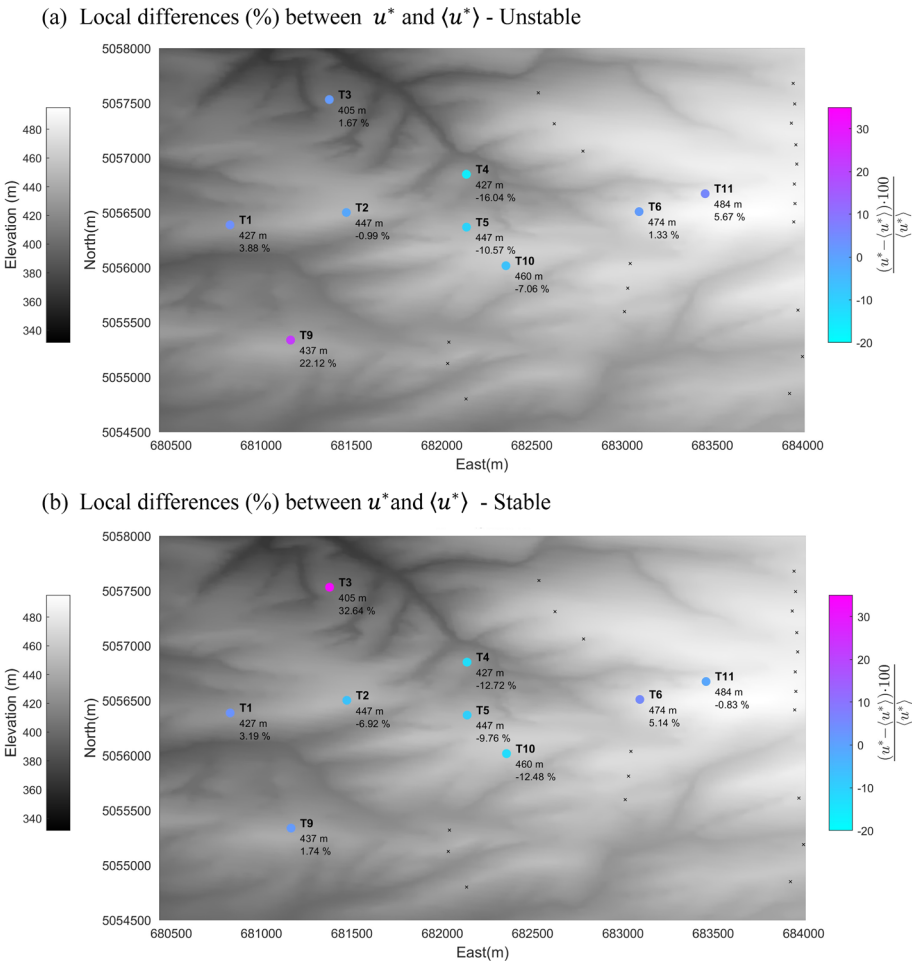


**Fig. 15** Topography of instrumented region (grayscale) and tower sites with annotated terrain elevation. The percentual differences between local and spatially averaged friction velocity at z = 10 m are shown for all sites. **a** Corresponds to UN periods between 12:00 and 15:00 PST for the observational period. **b** Same as before, but for Stable periods between 00:00 and 03:00 PST

## 4.2 Fluxes Horizontal Variability

For convenience, a 10% threshold (Sect. 3.3) was used to identify the towers that had local fluxes ($\overline{u'w'}$, $\overline{w'T'}$) higher or lower than their spatially averaged values. For a given stability regime (UN, N or S), both ($\overline{u'w'}$) and ($\overline{w'T'}$) exhibited similar deviations with respect to their spatially averaged values, ($\langle \overline{u'w'} \rangle$) and ($\langle \overline{w'T'} \rangle$), across all tower sites. Like what we observed for the CFL validity, the highest horizontal variability for the longitudinal momentum flux ($\overline{u'w'}$) was reported for the UN regime, while the highest horizontal variability for the temperature flux ($\overline{w'T'}$) was reported for the S regime.

During N, local deviations were less than $\pm$ 10% of the spatially averaged fluxes most of the time, but the number of N cases were infrequently reported compared to the UN

and S regimes. Finally, the tower T11 exhibited unique behaviour for $\overline{u'w'}$ and $\overline{w'T'}$, where systematically higher (or lower) values were observed locally when compared to the rest of the towers, which calls for more detailed studies to investigate subgrid variability in complex terrain when the local topographic variability is high. The average slope from the foothill to T11 in the windward face was much higher (~ 15%) compared to all other towers (~ 8%), and the configuration at T11 may have a propensity for flow separation, likely due to differences in surface roughness and the presence of upstream terrain heterogeneities where flow could pool during low wind and stable conditions. According to Walmsley and Taylor (1996), linear theories for complex terrain flows perform better for low slopes ($\leq 17°$), implying flow separation and non-linear effects become important for large slopes.

### 4.3 Atmospheric Surface layer (ASL) Parameterizations

The influence of surface heterogeneity on flow and turbulence is a topic of continuing interest (Stoll et al. 2020). Because of high flow variability, stability dependence of meteorology and logistical constraints, complex-terrain field campaigns have not provided a clear delineation of heterogeneity effects on ASL (Maronga and Raasch 2013). Only a few field experiments have recorded the characteristics of flow at high horizontal resolutions in complex terrain (Eder et al. 2015; Fernando et al. 2015, 2019), and our present knowledge is largely derived from very high horizontal resolution Large-Eddy-Simulations (LES) that has become the tool of choice for ASL studies (Chow et al. 2019; Stoll et al. 2020). Our observations showed that the highest flow heterogeneity (lowest parameterization scheme performance) occurs during UN conditions. Rai et al. (2017) used LES to study the convective boundary layer and found that horizontal gradients play a key role in the total TKE budgets in complex terrain. LES of Maronga and Raasch (2013) found that surface heterogeneities may lead to 'roll-like' secondary circulations when wind speeds are in the range 3–6 m $s^{-1}$, which look like 'updrafts' and 'downdrafts' across a horizontal plane; this was used to explain the heterogeneous distribution of sensible heat flux. In our study, such features were not recorded, even though the instrumentation was capable of doing so. We found that (i) flow heterogeneity may explain errors in a widely used mesoscale model parameterization scheme, and (ii) that under certain meteorological conditions (westerly winds > 5 m $s^{-1}$), flow heterogeneity (a time-dependent parameter) in the complex terrain considered may become comparable to that of flat terrain. Thus, the skill of parameterization schemes in mesoscale models can be quite effective in both cases. Our findings call for more detailed field campaigns to study subgrid variability in complex terrain. Our instrumental layout could be improved in the future by choosing a uniform spacing between towers to avoid possible biases when spatially averaging the results, as well as by including measurements in both ridges and low-laying areas. In addition, areas where the terrain exhibits strong directional anisotropies should be avoided in future studies, unless high-resolution LES simulations or spatially resolved measurements (e.g. Scanning Lidars) are available and properly configured. Finally, choosing fully developed and well characterized vertical profiles (e.g., by using temperature and velocity profilers) upstream of the subgrid topography is highly recommended in this kind of studies, as well as a proper characterization of the surface roughness and soil characteristics when considering extensive measurement periods (e.g., seasons to years).

## 5 Summary and Conclusions

In this article, we investigated the spatial variability of SL parameters including the stability parameter ($z/L^*$) and the turbulent heat and momentum fluxes ($\overline{wT}$ and $\overline{uw}$, respectively) over horizontal scales that are not properly resolved (subgrid) by NWP models and for an area of heterogeneous terrain located in the vicinity of the Columbia River in the U.S. Pacific Northwest. In addition, we explored the validity of the Constant-Flux Layer (CFL) and the skill of a SL parameterization based on Monin–Obukhov (MO) theory. The data used in this study was representative of the late summer/early fall meteorology in the region. The measurements were quality controlled for outliers, and to minimize disturbances from tower's booms and wake effects from wind turbines located in the eastern part of the domain, only winds in the sector 240°- 290° were considered in the results of Sects. 3.2–3.4.

Our analysis showed that the validity of the CFL concept was dependent on: (i) the turbulent parameter being analysed, (ii) the measurement's location (along the east–west transect), (iii) the atmospheric stability regime, and (iv) the magnitude of the flux. To evaluate the validity of the CFL for the momentum and temperature fluxes, we adopted a 10% threshold based on a previous study in complex terrain (Sfyri et al. 2018). As stated in the introduction, even when the CFL is satisfied, vertical gradients near the ground can be very high, however, our results showed that by choosing a sufficiently thin layer (i.e., 7 m), the changes in the fluxes across this layer can be quite small. The relationship between the validity of the CFL and the vertical gradients of turbulent fluxes an higher-order moments is still a subject of great interest to ASL studies (Li et al. 2018).

Monin-Obukhov (MO) equations used in WRF SL option 2 (Jiménez et al. 2012) were used to simulate time series of friction velocity for 27 August to 26 September 2016. MO theory assumes the existence of a CFL and horizontally homogeneity of flow. Naturally, the expectation was that MO would fail in view of terrain heterogeneity. Higher errors in the SL scheme were associated with high flow heterogeneity, as quantified by the Mean Absolute Deviation (MAD) between the simulated and observed friction velocity. Notwithstanding, on the days with transitional westerly winds ($> 5$ m s$^{-1}$), the parameterization scheme predicted the observed friction velocity remarkably well ($< 20\%$ errors).

This paper is dedicated to the memory of a prominent meteorologist and an excellent mentor Professor Sergej S. Zilitinkevich, and it is written for this Special Issue in his honour. For over 50 years, Prof. Sergej Zilitinkevich carried out pioneering research on atmospheric turbulence and planetary boundary layer (PBL). Among his numerous outstanding achievements in atmospheric boundary layer theory, a few results should be highlighted in relation to this study. At the end of the 1960s, Zilitinkevich and Chalikov (1968) proposed a simple linear interpolation (log-linear law) for the non-dimensional vertical gradient of mean wind speed (6) that provides blending between neutral and very stable ('$z$-less') cases. The WRF modelers undoubtedly appreciate Sergej's works through the "$C_{zil}$ coefficient", which represents the coupling between the aerodynamic $z_0$ (see Eq. 4) and scalar $z_{0t}$ (e.g., temperature and water vapour) roughness lengths (Zilitinkevich 1970; Zilitinkevich et al. 1992, 2001 and references therein). Here it is impossible not to mention some of his other achievements and contributions to the field: the depth of the stably stratified PBL, the resistance and heat and mass transfer laws for geophysical turbulent flows (Zilitinkevich 1970), non-local theory of the atmospheric PBL (e.g., Zilitinkevich et al. 2006), and higher-order turbulence parameterization schemes (Zilitinkevich et al. 2013), to name a few.

**Acknowledgements** University of Notre Dame contribution to WFIP2 project was funded by the grant DOE-WFIFP2-SUB-001. The work appearing in this paper was supported by the US National Science Foundation

Award AGS-1921554. The authors would like to thank the reviewers and editor for their valuable feedback during the peer-review process, which helped improve the overall quality of the manuscript. Finally, we would like to express our gratitude to Paolo Gianni from the University of Notre Dame, who provided thoughtful and valuable feedback that contributed to this manuscript.

**Data availability** The datasets analysed during the current study are available in the WFP2 repository of the Atmosphere to Electrons Data archive of the U.S. Department of Energy and is publicly available to download at https://a2e.energy.gov/projects/wfip2

## Appendix

See Figs 16,17,18,19,20,21,22, 23.

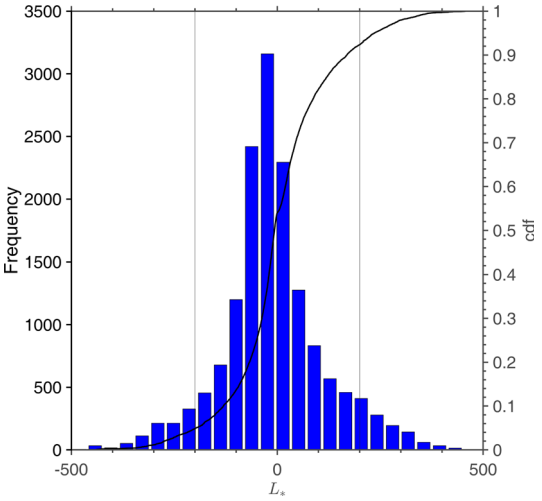


**Fig. 16** Histogram of the Obukhov length scale using the combined measurements from all tower sites at z = 10 m agl. The two vertical lines show the lower and upper thresholds used to identify Near-Neutral (NN) cases ($L_{TR} = 200$). This distribution corresponds to the wind sector (240, 290)

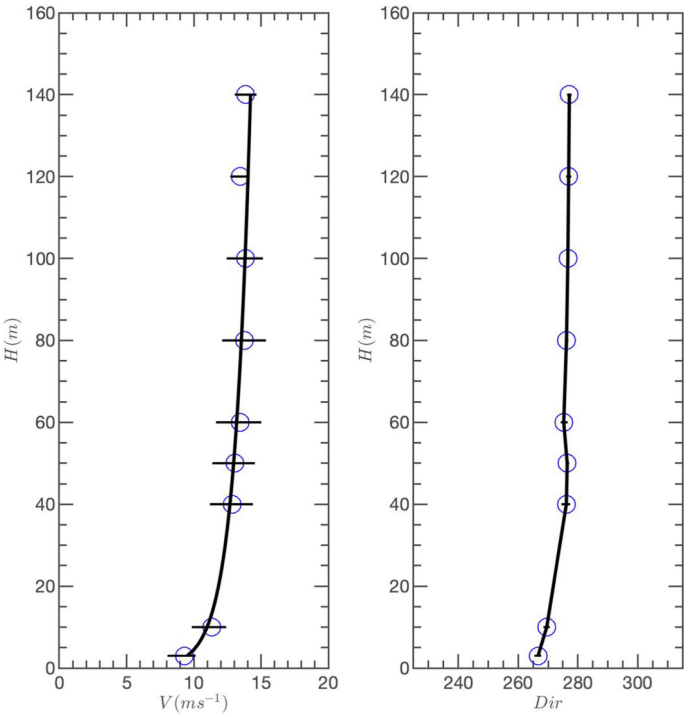


**Fig. 17** Wind speed and wind direction profiles from the combined measurements from the tower and the Sodar at site T1 that were used to estimate the roughness length value. This profile was aggregated for multiple periods with Near-Neutral (NN) conditions and the measured standard deviation is indicated by the black horizontal lines

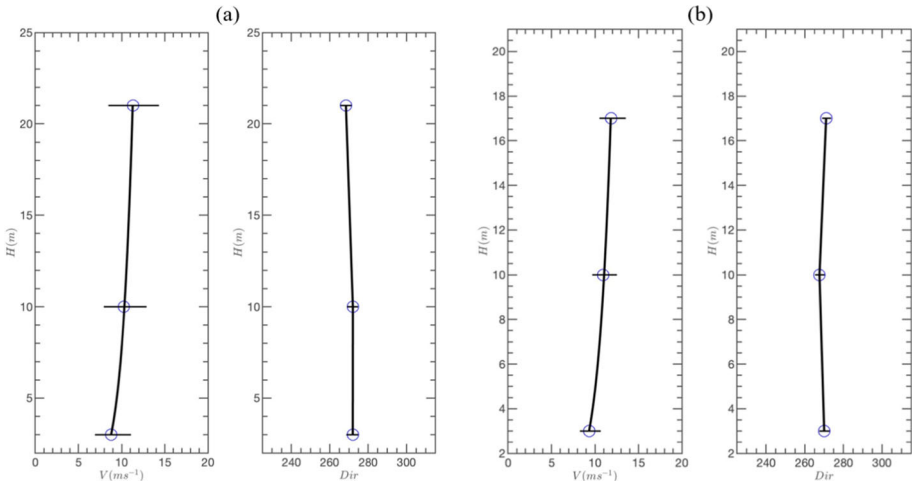


**Fig. 18** Aggregated **a** wind speed and wind direction profiles measured at site T2 for NN conditions and used to calculate the roughness length at site T2, and **b** Same as in **a** but for site T6. The standard deviation is indicated by the black horizontal line

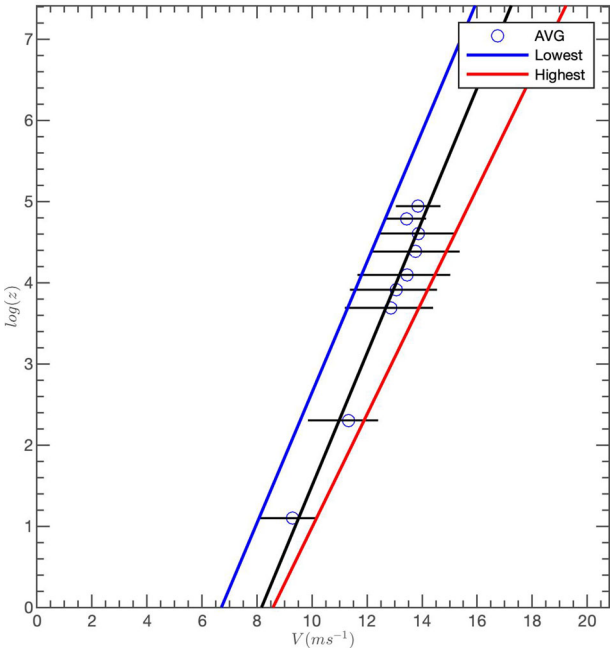


**Fig. 19** An example of the methodology proposed by Panofsky (1962) to determine roughness length. The methodology was applied to the velocity profiles measured at site T1 (as shown in Fig. A. 2)

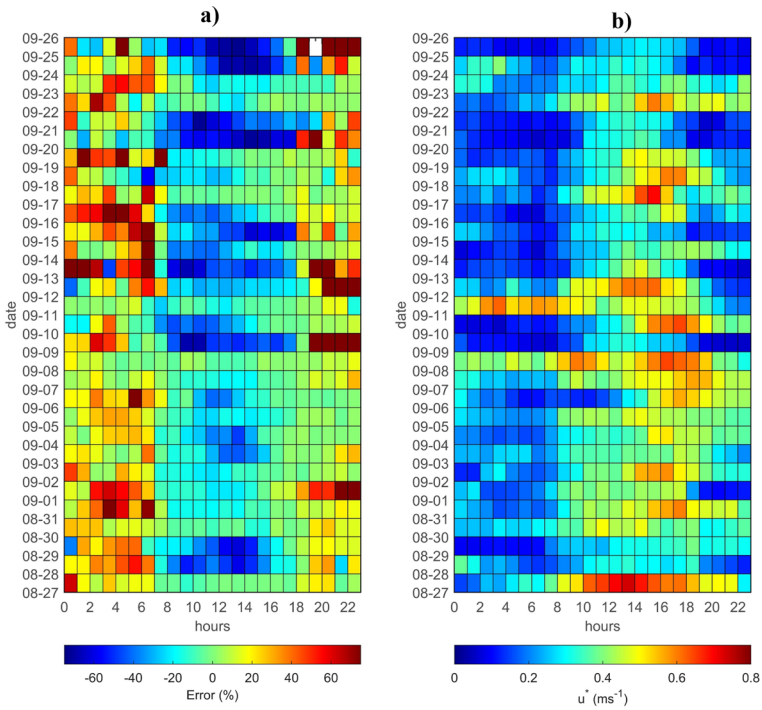


**Fig. 20** Color maps of **a** 1 h Error (%) between observed and simulated friction velocities; and **b** 1 h observed friction velocity for the period 27 August 2016 to 26 September 2016. The abscissa indicates the local time whereas the ordinate is the date

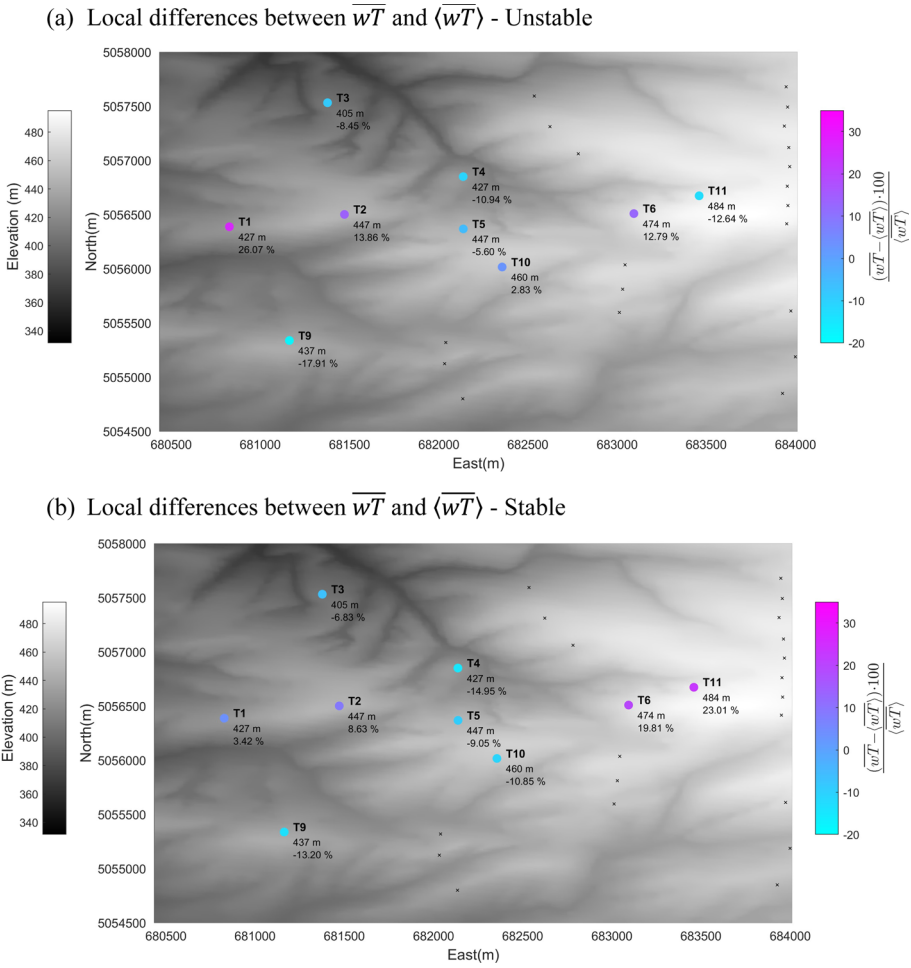


**Fig. 21** Topography of instrumented region (grayscale) and tower sites with annotated terrain elevation. The percentual differences between local and spatially averaged temperature fluxes at z = 10 m are shown for all sites. **a** Corresponds to UN periods between 12:00 and 15:00 PST for the observational period. **b** Same as before, but for Stable periods between 00:00 and 03:00 PST

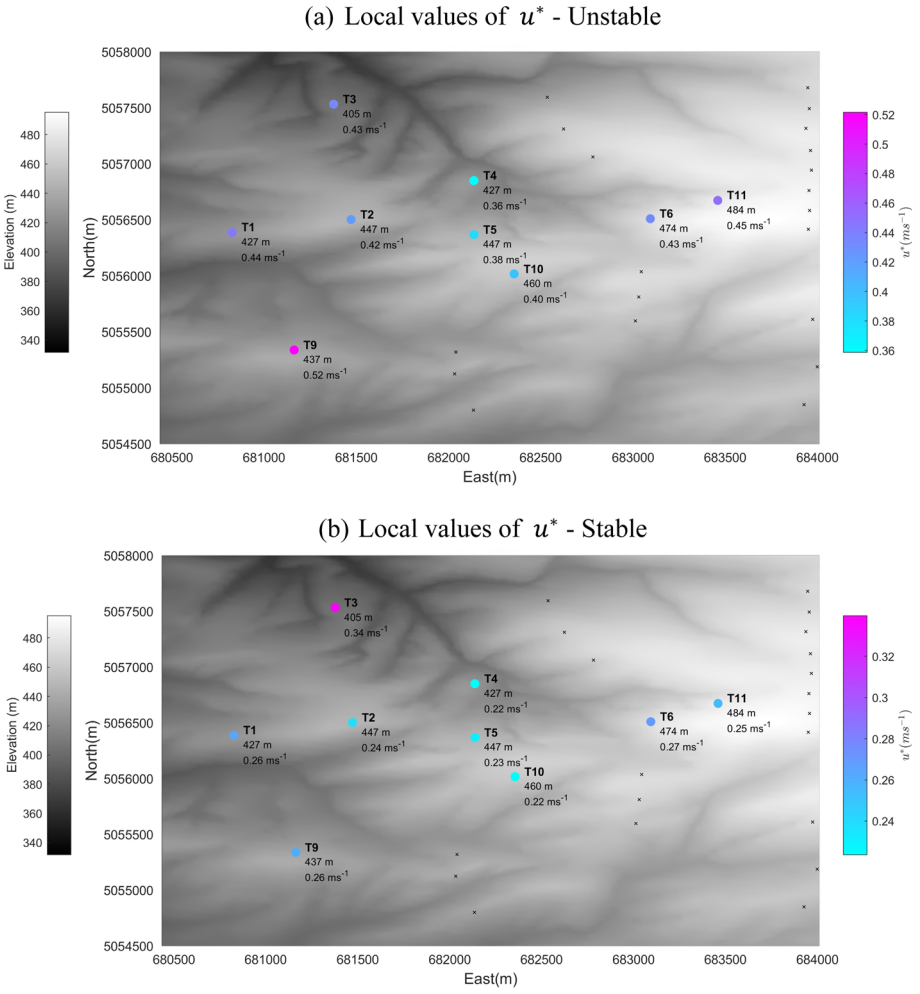


**Fig. 22** Topography of instrumented region (grayscale) and tower sites with annotated terrain elevation. Local values of friction velocity ($u^*$) at z = 10 m are shown for all sites. **a** Corresponds to UN periods between 12:00 and 15:00 PST for the observational period. **b** Same as before, but for Stable periods between 00:00 and 03:00 PST

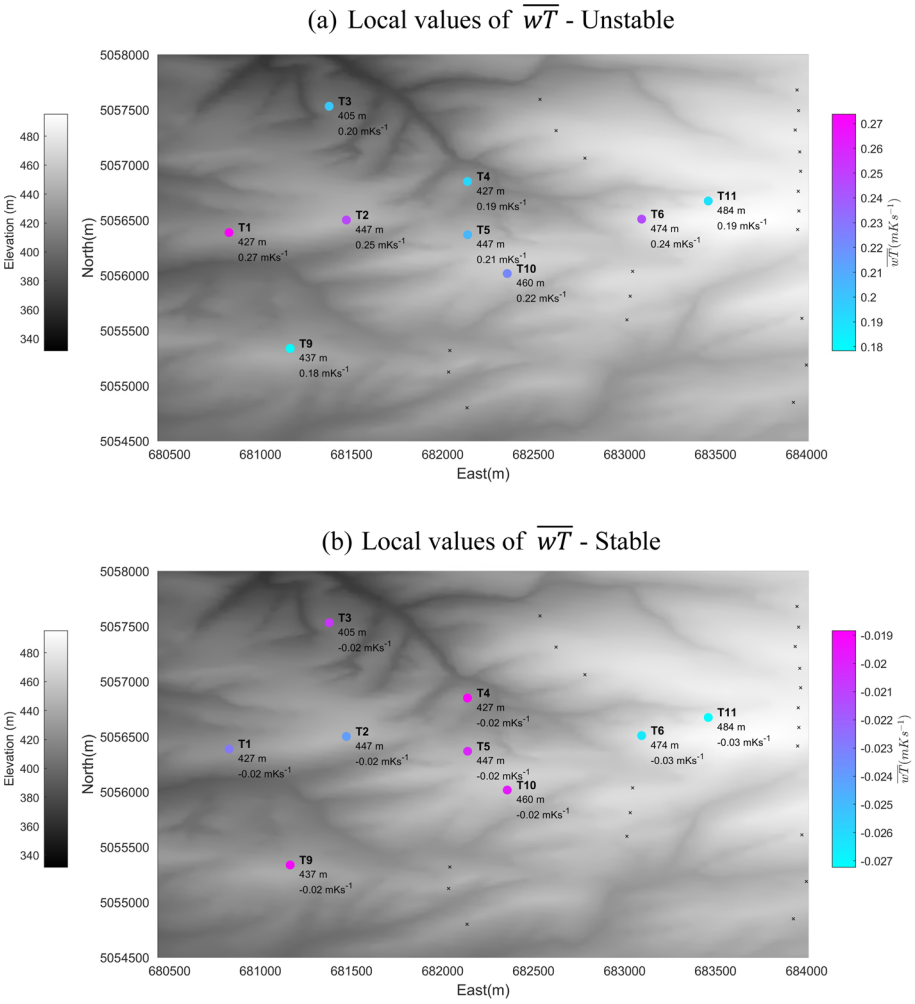


**Fig. 23** Topography of instrumented region (grayscale) and tower sites with annotated terrain elevation. Local values of temperature fluxes ($\overline{wT}$) at z = 10 m are shown for all sites. a Corresponds to UN periods between 12:00 and 15:00 PST for the observational period. b Same as before, but for Stable periods between 00:00 and 03:00 PST

## References


Bodini N, Lundquist JK, Krishnamurthy R, Pekour M, Berg LK, Choukulkar A (2019) Spatial and temporal variability of turbulence dissipation rate in complex terrain. Atmos Chem Phys 19(7):4367–4382

Carvalho L, Duine GJ, Jones C et al (2020) The sundowner winds experiment (SWEX) pilot study: understanding downslope windstorms in the Santa Ynez Mountains, Santa Barbara, California. Mon Weather Rev 148:1519–1539. https://doi.org/10.1175/MWR-D-19-0207.1

Chow FK, Schär C, Ban N, Lundquist KA, Schlemmer L, Shi X (2019) Crossing multiple gray zones in the transition from mesoscale to microscale simulation over complex terrain. Atmosphere 10(5):274

Chung U, Seo HH, Hwang KH et al (2006) Minimum temperature mapping over complex terrain by estimating cold air accumulation potential. Agric for Meteorol 137:15–24. https://doi.org/10.1016/j.agrformet.2005.12.011

Eder F, Schmidt M, Damian T et al (2015) Mesoscale eddies affect near-surface turbulent exchange: evidence from lidar and tower measurements. J Appl Meteorol Climatol 54:189–206. https://doi.org/10.1175/JAMC-D-14-0140.1

Fernando HJS (2010) Fluid dynamics of urban atmospheres in complex terrain. Annu Rev Fluid Mech 42:365–389. https://doi.org/10.1146/annurev-fluid-121108-145459

Fernando HJS, Pardyjak ER, Di Sabatino S et al (2015) Unraveling the intricacies of mountain weather. Bull Am Meteorol Soc. https://doi.org/10.1175/BAMS-D-13-00131.1

Fernando HJS, Mann J, Palma JMLM et al (2019) The perdigao peering into microscale details of mountain winds. Bull Am Meteorol Soc. https://doi.org/10.1175/BAMS-D-17-0227.1

Garratt J (1994) The atmospheric boundary layer. Earth Sci Rev 37(1–2):89–134. https://doi.org/10.1007/3-211-38078-7_4

Giovannini L, Ferrero E, Karl T et al (2020) Atmospheric pollutant dispersion over complex terrain: challenges and needs for improving air quality measurements and modeling. Atmosphere (basel) 11:1–32. https://doi.org/10.3390/atmos11060646

Grachev AA, Fairall CW, Blomquist BW, Fernando HJS, Leo LS, Otárola-Bustos SF, Wilczak JM, McCaffrey KL (2020) On the surface energy balance closure at different temporal scales. Agric Forest Meteorol. https://doi.org/10.1016/j.agrformet.2019.107823

Grachev AA, Fairall CW, Blomquist BW, Fernando HJ, Leo LS, Otárola-Bustos SF, McCaffrey KL (2022) A hybrid bulk algorithm to predict turbulent fluxes over dry and wet bare soils. J Appl Meteorol Climatol 61(4):393–414

Grell GA, Dudhia J, Stauffer DR (1995) A Description of the Fifth- Generation Penn State/NCAR Mesoscale Model (MM5) NCAR Technical Note, NCAR/TN-398+STR, Boulder, CO., 138 pp

Gultepe I, Sharman R, Williams PD et al (2019) A review of high impact weather for aviation meteorology. Pure Appl Geophys 176:1869–1921. https://doi.org/10.1007/s00024-019-02168-6

Haupt SE, Kosovic B, Shaw W et al (2019) On bridging a modeling scale gap: mesoscale to microscale coupling for wind energy. Bull Am Meteorol Soc 100:2533–2549. https://doi.org/10.1175/BAMS-D-18-0033.1

Hong S-Y, Dudhia J (2012) Next-generation numerical weather prediction: bridging parameterization, explicit clouds, and large eddies. Bull Am Meteorol Soc 93:ES6–ES9. https://doi.org/10.1175/2011bams3224.1

Jiménez PA, Dudhia J, González-Rouco JF et al (2012a) A revised scheme for the WRF surface layer formulation. Mon Weather Rev 140:898–918. https://doi.org/10.1175/MWR-D-11-00056.1

Kadivar M, Tormey D, McGranaghan G (2021) A review on turbulent flow over rough surfaces: fundamentals and theories. Int J Thermofluids 10:100077

Kaimal JC, Businger JA (1970) Case studies of a convective plume and a dust devil. J Appl Meteorol Climatol 9(4):612–620

Klipp CL, Mahrt L (2004) Flux–gradient relationship, self-correlation and intermittency in the stable boundary layer. Quart J R Meteorol Soc J Atmosph Sci Appl Meteorol Phys Oceanogr 130(601):2087–2103

Li D, Katul GG, Liu H (2018) Intrinsic constraints on asymmetric turbulent transport of scalars within the constant flux layer of the lower atmosphere. Geophys Res Lett 45(4):2022–2030

Liang J, Guo Q, Zhang Z et al (2020) Influence of complex terrain on near-surface turbulence structures over loess plateau. Atmosphere Basel. https://doi.org/10.3390/atmos11090930

Luchetti NT, Friedrich K, Rodell CE, Lundquist JK (2020) Characterizing thunderstorm gust fronts near complex terrain. Mon Weather Rev 148:3267–3286. https://doi.org/10.1175/MWR-D-19-0316.1

Maronga B, Raasch S (2013) Large-eddy simulations of surface heterogeneity effects on the convective boundary layer during the LITFASS-2003 experiment. Boundary-Layer Meteorol 146:17–44. https://doi.org/10.1007/s10546-012-9748-z

Maronga B, Knigge C, Raasch S (2020) An improved surface boundary condition for large-eddy simulations Based on Monin-Obukhov similarity theory: evaluation and consequences for grid convergence in neutral and stable conditions. Boundary Layer Meteorol 174:297–325. https://doi.org/10.1007/s10546-019-00485w

Martins CA, Moraes OLL, Acevedo OC, Degrazia GA (2009) Turbulence intensity parameters over a very complex terrain. Boundary-Layer Meteorol 133:35–45. https://doi.org/10.1007/s10546-009-9413-3

Monin AS, Obukhov AM (1954) Basic laws of turbulent mixing in the surface layer of the atmosphere. Contrib Geophys Inst Acad Sci USSR 151(163):e187

Moraes OL, Acevedo OC, Degrazia GA, Anfossi D, da Silva R, Anabor V (2005) Surface layer turbulence parameters over a complex terrain. Atmos Environ 39(17):3103–3112

Muñoz-Esparza D, Cañadillas B, Neumann T, Van Beeck J (2012) Turbulent fluxes, stability and shear in the offshore environment: mesoscale modelling and field observations at FINO1. J Renew Sustain Energy. https://doi.org/10.1063/1.4769201

Nadeau DF, Pardyjak ER, Higgins CW, Parlange MB (2013) Similarity scaling over a steep alpine slope. Boundary Layer Meteorol 147:401–419. https://doi.org/10.1007/s10546-012-9787-5

Nakanishi M, Niino H (2009) Development of an improved turbulence closure model for the atmospheric boundary layer. J Meteorol Soc Japan 87:895–912. https://doi.org/10.2151/jmsj.87.895

Obukhov A (1946) Turbulence in thermally inhomogeneous atmosphere. Trudy Inst Teor Geofiz Akad Nauk SSSR 1:95–115

Panofsky A. Determination of stress from wind. Q J R Meteorol Soc, (1962)

Panofsky HA, Dutton JA (1984) Atmospheric turbulence—models and methods for engineering applications. Wiley, New York, p 397

Pope SB, Pope SB (2000) Turbulent flows. Cambridge University Press

Rai RK, Berg LK, Pekour M et al (2017) Spatiotemporal variability of turbulence kinetic energy budgets in the convective boundary layer over both simple and complex terrain. J Appl Meteorol Climatol 56:3285–3302. https://doi.org/10.1175/JAMC-D-17-0124.1

Sati AP, Mohan M (2021) Impact of urban sprawls on thunderstorm episodes: Assessment using WRF model over central-national capital region of India. Urban Clim 37:100869. https://doi.org/10.1016/j.uclim.2021.100869

Sfyri E, Rotach MW, Stiperski I et al (2018) Scalar-flux similarity in the layer near the surface over mountainous terrain. Boundary Layer Meteorol 169:11–46. https://doi.org/10.1007/s10546-018-0365-3

Skamarock WC, Klemp JB, Dudhia J, Gill DO, Barker DM, Duda MG, Huang X-Y, Wang W, Powers JG. A Description of the Advanced Research WRF Version 3, National Center for Atmospheric Research Technical Note NCAR, Boulder (2008) http://www.mmm.ucar.edu/wrf/users/docs/arw_v3.pdf

Stoll R, Gibbs JA, Salesky ST et al (2020) Large-eddy simulation of the atmospheric boundary layer. Boundary Layer Meteorol 177:541–581. https://doi.org/10.1007/s10546-020-00556-3

Stull RB (1988) An introduction to boundary layer meteorology, vol 13. Springer Science and Business Media

Tampieri F, Maurizi A, Viola A (2009) An investigation on temperature variance scaling in the atmospheric surface layer. Boundary Layer Meteorol 132(1):31–42

Walmsley JL, Taylor PA (1996) Boundary-layer flow over topography: impacts of the Askervein study. Boundary Layer Meteor 78(34):291–320. https://doi.org/10.1007/BF00120939

Wilczak JM, Oncley SP, Stage SA (2001) Sonic anemometer tilt correction algorithms. Boundary Layer Meteorol 99(1):127–150

Wilczak JM et al (2019) The second wind forecast improvement project (WFIP2): observational field campaign. Bull Am Meteor Soc. https://doi.org/10.1175/BAMS-D-18-0035.1

Wouters H, de Ridder K, van Lipzig NPM (2012) Comprehensive parametrization of surface-layer transfer coefficients for use in atmospheric numerical models. Boundary Layer Meteorol 145:539–550. https://doi.org/10.1007/s10546-012-9744-3

Wyngaard JC (2011) The atmospheric surface layer. Turbul Atmos. https://doi.org/10.1017/cbo9780511840524.011

Zilitinkevich SS (1970) Dynamics of the atmospheric boundary layer. Gidrometeoizdat, Leningrad, p 290

Zilitinkevich SS, Chalikov DV (1968) The laws of resistance and of heat and moisture exchange in the interaction between the atmosphere and an underlying surface. Izv Acad Sci USSR Atmos Ocean Phys 4:765–772

Zilitinkevich SS, Fedorovich EE, Shabalova MV (1992) Numerical model of a non-steady atmospheric planetary boundary layer, based on similarity theory. Boundary Layer Meteorol 59(4):387–411. https://doi.org/10.1007/BF02215460

Zilitinkevich SS, Grachev AA, Fairall CW (2001) Scaling reasoning and field data on the sea-surface roughness lengths for scalars. J Atmos Sci 58(3):320–325

Zilitinkevich SS, Hunt JCR, Esau IN, Grachev AA, Lalas DP, Akylas E, Tombrou M, Fairall CW, Fernando HJS, Baklanov AA, Joffre SM (2006) The influence of large convective eddies on the surface layer turbulence. Quart J Roy Met Soc 132(618A):1423–1456. https://doi.org/10.1256/qj.05.79

Zilitinkevich SS, Elperin T, Kleeorin N, Rogachevskii I, Esau I (2013) A hierarchy of energy—and flux-budget (FEB) turbulence closure models for stably-stratified geophysical flows. Boundary Layer Meteorol 146(3):341–373. https://doi.org/10.1007/s10546-012-9768-8